

1 **Observed variability of the North Atlantic Current in the Rockall Trough from four years of**
2 **mooring measurements**

3

4 **L. Houpert¹, S. Cunningham², N. Fraser², C. Johnson², N. P. Holliday¹, S. Jones²,**
5 **B. Moat¹, D. Rayner¹**

6 ¹National Oceanography Centre, Southampton, UK

7 ²Scottish Association for Marine Science, Oban, UK

8

9 Corresponding author: Loïc Houpert (loic.houpert@noc.ac.uk)

10

11 **Key Points**

- 12 • Around half of the northward transport of the warm North Atlantic Current (NAC),
13 flows through the Rockall Trough
- 14 • The first continuous observations of Rockall Trough transport show that 6.6 Sv is
15 carried northward in the NAC.
- 16 • High northward transport is characterised by a strong NAC jet in the Rockall
17 Trough; weak transport by mesoscale eddy activity

18

19

20

21

22

23

24 **Abstract**

25 The Rockall Trough is one of the main conduits for warm Atlantic Water to the
26 Nordic Seas. Ocean heat anomalies, originating from the eastern subpolar gyre, are
27 known to influence Arctic sea ice extent, marine ecosystems, and continental climate.
28 Knowledge of the transport through this basin has previously been limited to estimates
29 from hydrographic sections which cannot characterise the intra-annual and multi-annual
30 variability. As part of the Overturning in the Subpolar North Atlantic Programme
31 (OSNAP), a mooring array was deployed in the Rockall Trough in order to obtain the
32 first continuous measurements of transport. Here, we define the methodology and the
33 errors associated with estimating these transports. Results show a 4-year mean
34 northward transport of 6.6 Sv (1 Sv = 10^6 m³/s) by the North Atlantic Current (NAC) in
35 the east and interior of the Rockall Trough (2014-2018). A mean transport of -2.0 Sv
36 (southward) is observed in the west of the basin, which could be part of a recirculation
37 around the Rockall Plateau. The 90-day low-pass filtered transport shows large
38 sub-annual and inter-annual variability (-1.6 Sv to 9.1 Sv), mostly resulting from
39 changes in the mid-basin geostrophic transport. Satellite altimetry reveals the periods of
40 low and high transport are associated with significant changes in the Rockall Trough
41 circulation. There is a detectable seasonal signal, with the greatest transport in spring
42 and autumn.

43

44

45 **Plain Language Summary**

46 There is mounting evidence that the North Atlantic Current (eastward extension of the
47 Gulf Stream) heavily influences the European and Arctic climate. To adequately
48 measure this current and understand its dynamics, an array of underwater instruments
49 was deployed in the Rockall Trough, a remote region of the eastern North Atlantic. Over
50 a four-year period, these instruments continuously collected measurements of
51 temperature, salinity, pressure and velocity data. Analysis of these data provides a new
52 and more accurate description of the North Atlantic Current in this region. This study
53 reveals a surprisingly large variability in the eastern North Atlantic circulation. The

54 combined analysis of satellite data indicates that this variability is due to changes of the
55 North Atlantic Current system.

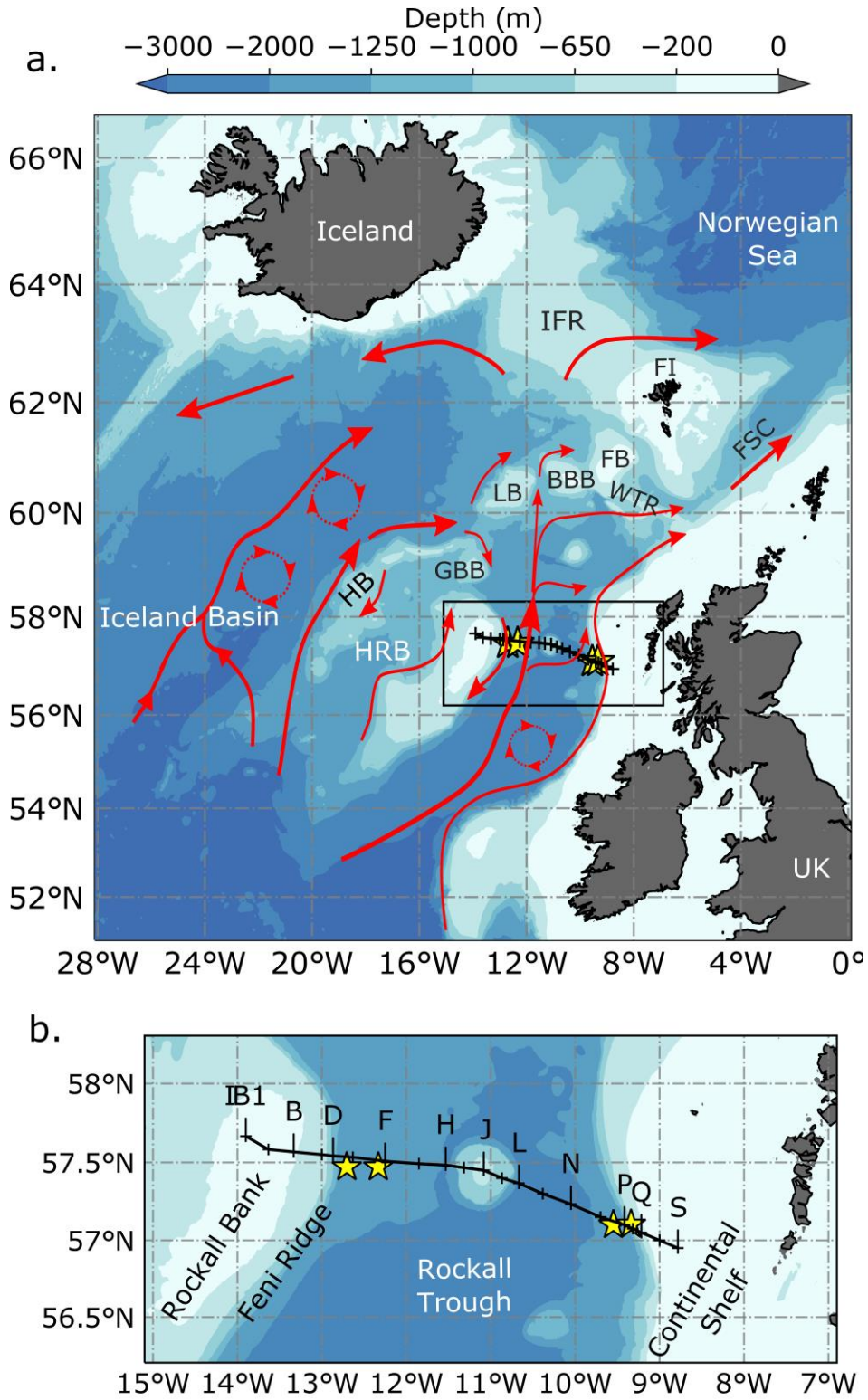
56 **1 Introduction**

57 In 2014, the Overturning in the Subpolar North Atlantic Programme (OSNAP)
58 established an array of more than fifty moorings across the subpolar North Atlantic, with
59 the objective of continuously measuring the strength, structure and variability of the
60 circulation. The array is able to diagnose both the horizontal and overturning circulations
61 and their associated fluxes of heat and fresh-water. The programme combines
62 measurements of the temperature, salinity and directly measured currents, with salinity
63 and temperature fields derived from purposefully deployed ocean gliders, Argo floats
64 and hydrographic cruises, with satellite altimetry and mass balance constraints.

65 Results from the first 21 months of the array (August 2014 to April 2016) were
66 reported in Lozier et al. (2019) and provide remarkable evidence that the majority of the
67 overturning occurs north of the OSNAP_{east} section between East Greenland and
68 Scotland. The Atlantic Meridional Overturning Circulation (AMOC) strength at
69 OSNAP_{east} is 15.6 ± 0.8 Sv ($1 \text{ Sv} = 10^6 \text{ m}^3/\text{s}$) compared to only 2.1 ± 0.3 Sv in the
70 Labrador Sea north of OSNAP_{west}. The zonally-integrated meridional volume fluxes
71 along OSNAP_{east} show that there is 12.2 Sv of upper-limb transport associated with the
72 North Atlantic Current (NAC, defined as water with potential density $\sigma_0 < 27.66 \text{ kg/m}^3$).
73 Of this 12.2 Sv, OSNAP data show that 43% (5.2 Sv) of the flow is east of 13.0°W ,
74 through the Rockall Trough. From this 12.2 Sv of NAC transport, 58 to 69% is carried
75 poleward over the Greenland-Scotland Ridge (7.1-8.4 Sv) via the Iceland-Faroe Ridge,
76 the Faroe-Shetland slope current and the European Shelf (Berx et al., 2013; Hansen et
77 al., 2015; Østerhus et al., 2019; Rossby & Flagg, 2012; Figure 1).

78

79



80

81 Figure 1: Bathymetry and schematic of the North Atlantic upper-ocean circulation
82 ($\sigma_0 < 27.55 \text{ kg/m}^3$) over the 2014-2018 period (a) and bathymetry of the Rockall Trough
83 (b). Circulation schematic is based on absolute geostrophic current from altimetry
84 averaged over 2014-2018 (Figure S1), Houpert et al. (2018) for the Hatton-Rockall
85 Basin circulation, and the new results presented in this study. Altimetry-derived currents
86 are representative of the large-scale flow associated with the NAC branches, therefore
87 the circulation schematic drawn in the Rockall Trough is mostly representing a period of
88 high transport as defined in the manuscript by the high transport composite state. The
89 black box indicates the region shown on (b). UK-OSNAP moorings are indicated by
90 yellow stars and the Extend Ellet Line hydrographic stations used in this study are
91 indicated by black crosses and labelled on (b). Acronyms: IFR = Iceland-Faroe Ridge,
92 FI = Faroe Islands, FB = Faroe Bank, FSC = Faroe-Shetland Channel, LB = Lousy
93 Bank, BBB = Bill Bailey Bank, WTR = Wyville Thomson Ridge, HB = Hatton Bank, GBB
94 = George Bligh Bank, HRB = Hatton-Rockall Basin

95

96

97 The OSNAP Rockall Trough mooring array (Figure 2a) is designed to quantify the
98 transport of northward-flowing warm and saline water, and the magnitude of the
99 southward-flowing cold overflow water across the Wyville Thomson Ridge (Johnson et
100 al., 2017). The location and the multi-decadal context are determined by the
101 long-established Ellett Line section, 62 occupations in the Rockall Trough since 1975. In
102 1996, the hydrographic section was extended to Iceland and the Ellett Line project
103 became the Extended Ellett Line project (EEL). From 2018, the Rockall Trough mooring
104 array is funded under the Ellett Array project, under the Natural Environment Research
105 Council's National Capability programme CLASS (Climate Linked Atlantic Sector
106 Science, <https://projects.noc.ac.uk/class-project/>). The mooring array is complemented
107 by UK glider measurements across the Hatton-Rockall Basin (Houpert et al., 2018).

108 The Rockall Trough NAC branch is warmer and more saline than Iceland Basin NAC
109 branches, and contributes to the freshwater budgets and heat supply to the Nordic
110 Seas. Observations and models broadly agree on the mean structure and pathways but
111 the NAC's variability and branching structure is poorly understood (Hansen et al., 2008).
112 The variability of the strength and properties of the NAC are thought to be driven by the
113 horizontal expansion and contraction of the subpolar gyre due to multi-annual
114 thermohaline forcing (Häkkinen & Rhines, 2004; Hjálmar Hátún et al., 2005). When the
115 subpolar front retreats to the west, the temperature and salinity of upper waters in the

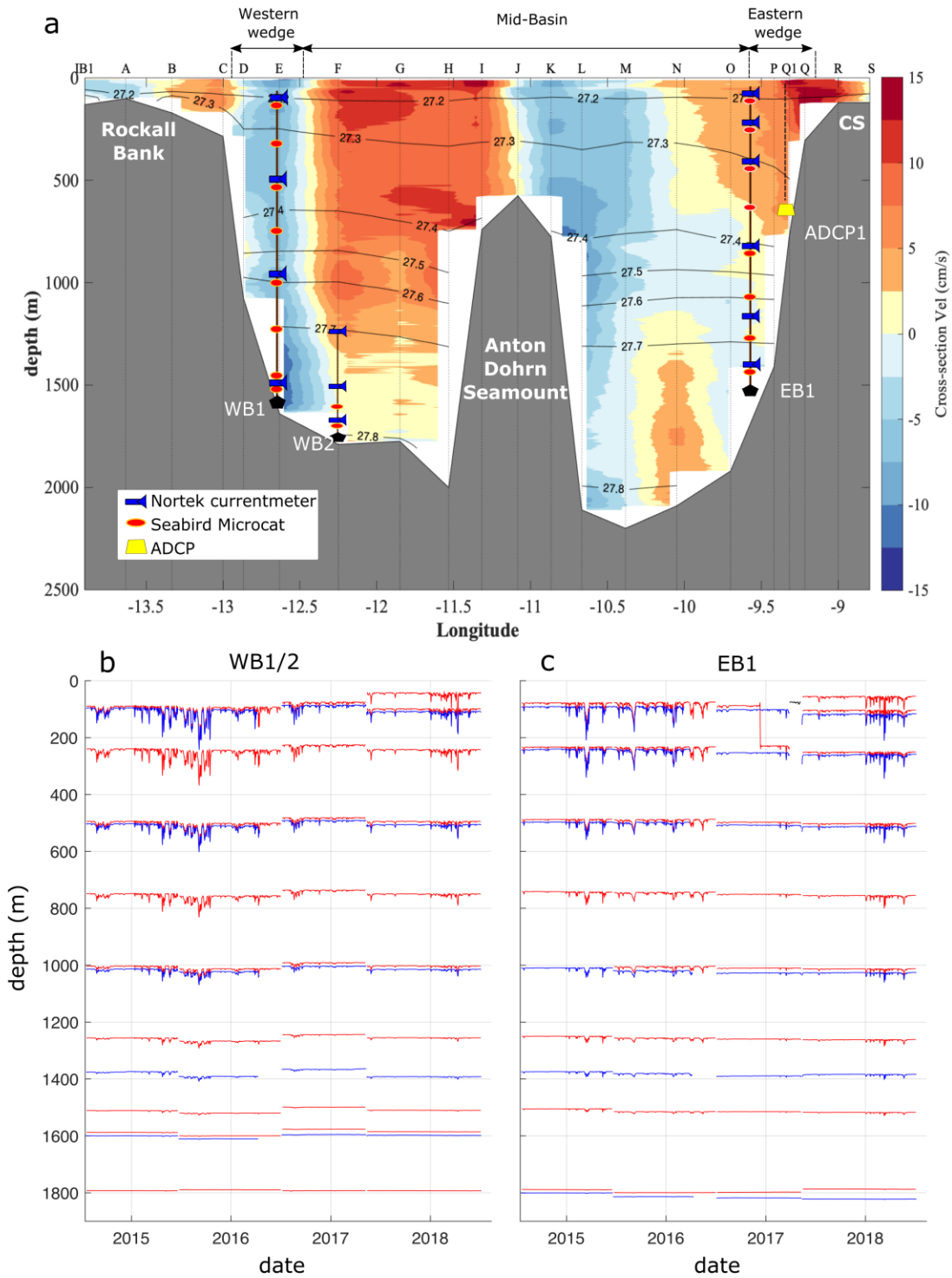
116 Rockall Trough increase, with these changes propagating into the Nordic Seas (Holliday
117 et al., 2008). Estimates of net northward transport through the Rockall Trough show that
118 it is contained in two main currents: a shelf edge current and a current in the interior of
119 the basin. The shelf edge current, found at depths <1000 m, is driven by the large-scale
120 density distribution of the north-eastern Atlantic (Huthnance, 1984; Marsh et al., 2017).
121 Variability of the shelf edge current on inter-annual timescales is likely due to changes
122 to the large-scale density distribution, particularly at the entrance to the Rockall Trough
123 (Holliday, 2003). On shorter timescales (seasonal and sub-seasonal), variations in wind
124 forcing are thought to dominate (Souza et al., 2001). A larger proportion of warm NAC
125 water flows northward through the basin interior. Estimates of transport from the Rockall
126 Trough part of the EEL sections are 3.7 ± 2.4 Sv (mean \pm standard deviation) between
127 1975 and 1998, and 3.0 ± 3.7 Sv between 1997 and 2014 (Holliday et al., 2000, 2015).
128 Gary et al. (2018) showed it is difficult to detect a seasonal cycle in the volume transport
129 from hydrographic observations because of high mesoscale variability. Thus, little is
130 known about the intra- and inter-annual variability associated with transport through the
131 Rockall Trough.

132 The Rockall Trough is separated from the Faroe-Shetland Channel by the Wyville
133 Thomson Ridge, limiting northward transport to depths <650 m (Figure 1). A net
134 southward transport of -0.3 Sv of Wyville Thomson Overflow Water has been detected
135 at the location of the EEL and mooring array (Johnson et al., 2010, 2017; Sherwin et al.,
136 2008).

137 In this paper we analyse four years of data (July 2014-July 2018) from the OSNAP
138 Rockall Trough mooring array, quantifying, for the first-time, the variability at
139 sub-seasonal, seasonal and interannual timescales. Firstly, we present the data which
140 is collected from instruments on the Rockall Trough moorings (Section 2), before
141 describing the methodology used to calculate the volume transports (Section 3). Next,
142 we make comprehensive estimates of the uncertainties that arise from our sampling
143 scheme, instrumental factors, processing methodologies and missing data (Section 4).
144 In Section 5 we describe and discuss the results in the context of historical
145 understanding of the circulation. The key issues are discussed in Section 6.

146

147



148 Figure 2: (a) Mean cross-section velocity from the 16 (summer) Extended Ellett Line
 149 LADCP sections in the Rockall Trough (1996-2017). Potential density anomalies (kg/m³)

150 are shown as black contour lines. The design of the UK-OSNAP mooring array
151 deployed since 2014 in the Rockall Trough is superimposed. The different sub-regions
152 used in the calculation of the volume flux are indicated on top. Acronym: CS,
153 Continental Shelf. (b) and (c) are the pressure time-series from the Rockall Trough WB
154 and EB mooring instruments used in this study. Sea-Bird SBE37 MicroCAT CTDs are
155 indicated in red, Nortek Aquadopp current meters in blue and reconstructed near-
156 surface instrument at EB1 from March to May 2017 in black (see Data section for more
157 details).

158

159 **2 Data**

160 **2.1 The Rockall Trough mooring array**

161 The array (Figure 2a) consists of three sub-surface taught wire moorings (WB1,
162 WB2 and EB1), and one Acoustic Doppler Current Profiler (ADCP) within a trawl
163 resistant frame (ADCP1). All moorings were first deployed in July 2014, except ADCP1
164 which was deployed in October 2014. The WB1, WB2 and EB1 moorings consist of
165 Sea-Bird SBE37 MicroCAT CTDs (measuring conductivity, temperature and pressure)
166 and Nortek Aquadopp current meters (measuring pressure and velocity). The pressure
167 time-series of the instruments are indicated in Figure 2b. All moorings were recovered
168 and redeployed in June 2015, July 2016, May 2017, and July 2018.

169 The two boundary currents in the west and east of the Rockall Trough are
170 measured directly using current meters. The sub-surface WB1 mooring (57.5 °N,
171 12.7 °W, water depth of 1600 m) was deployed to capture the narrow southward
172 boundary current seen in repeated Lowered Acoustic Doppler Current Profiler (LADCP)
173 sections (Figure 2a). This jet extends from 13.0 °W (EEL station C) to 12.5 °W (mid-way
174 between EEL stations E and F, Figure 2a). The EB1 sub-surface mooring (57.1 °N,
175 9.6 °W, water depth of 1800 m), and the ADCP mounted on trawl resistant frame
176 (57.1 °N, 9.3 °W, water depth of 750 m), were deployed in the eastern Rockall Trough
177 (Figure 1) to capture the shelf edge current extending from 9.6 °W to 9.2 °W (water
178 depth of 250 m) as seen on Figure 2a. The CTDs on WB1/WB2 and EB1 are used to
179 compute dynamic height profiles at the western and eastern boundary of the Rockall
180 Trough in order to compute the mid-basin geostrophic transport.

181 Data were processed using the methods developed for the RAPID array
182 (McCarthy et al., 2015; Rayner et al., 2011). Sea-Bird CTDs were calibrated pre and
183 post deployment by lowering on a CTD cast and instrument drifts were corrected.
184 Velocity data were corrected for magnetic deviations and speed of sound. Velocity and
185 CTD data were interpolated to a common timebase and filtered using a 40 hour
186 Butterworth filter to remove signals from tides and inertial oscillations. At each timestep,
187 we linearly interpolated the relatively sparse moored instrument data onto a high
188 resolution vertical grid (20 dbar grid). The errors due to this linear interpolation onto a
189 high resolution vertical grid is discussed in Supplementary Text S1. The surface gaps
190 were filled by linearly extrapolating the velocity profiles and the dynamic height profiles
191 to the surface.

192 Data return from the CTDs and current meters was very high as can be seen in
193 Figure 2b. Small losses have occurred due to battery failures and fishing damage to the
194 top of mooring EB1 between March and May 2017. In March 2017, the top 400 m of the
195 EB1 mooring broke due to fishing activities. Although the CTD and current meter
196 deployed at 100 m were later recovered from a Scottish Island, the CTD deployed at
197 250 m was lost. Data from the CTD at 100 m was used until the point at which the
198 mooring broke. After this (March 2017-May 2017), we reconstructed the temperature
199 and salinity using linear regressions with the time-series from 100 m at WB1 (correlation
200 coefficients of 0.93 for temperature and 0.85 for salinity over 2014-2016). The pressure
201 time-series associated with this reconstructed temperature and salinity at 100 m depth
202 on EB1 is shown in black on Figure 2c (more details in Text S1). Unfortunately, data
203 return from ADCP1 is limited to one 8-month deployment in 2014. All other deployments
204 failed despite the use of trawl-resistant frames. Several of the frames, minus the
205 ADCPs, have been recovered with evidence of trawling damage. Additionally, one
206 unrecoverable unit was filmed in situ on the seabed by a deep diving autonomous
207 submersible in July 2019. The lander was seen to be ploughed deeply into the mud and
208 extensively damaged, with the ADCP torn from the lander frame gimbal mount and lying
209 on the seabed. This lander was washed ashore in the Outer Hebrides in March 2020.
210 From 2020, gliders are deployed in the shelf edge current to provide continuous

211 observations between the 200m contour and the 2000m contour westward of the EB1
212 mooring.

213

214 **2.2 Ancillary Data**

215 LADCPs measure full-depth currents on CTD casts and have been deployed on
216 EEL hydrographic sections since 1996. Between 1996 and 2004 the instruments used
217 were 150 kHz broadband ADCPs and data were processed using software developed
218 by Eric Firing at the University of Hawaii. From 2005 onwards, 300 kHz broadband
219 ADCPs were used and their data were processed using the IX Lamont- Doherty Earth
220 Observatory software (Thurnherr, 2014). LADCP absolute velocities from both methods
221 have an uncertainty of 0.02-0.03 m/s (Holliday et al., 2009; Thurnherr, 2014). Data were
222 de-tided using barotropic tides at the time of each cast, obtained from the Oregon State
223 University Tidal Inversion Software (Egbert & Erofeeva, 2002; <https://www.tpxo.net/>).

224 We use gridded and along-track delayed mode data of daily global sea-level
225 anomalies, absolute sea-surface dynamic topography, surface absolute geostrophic
226 velocities and velocity anomalies at a spatial resolution of 0.25°. Data were obtained
227 from the SSALTO/DUACS (Segment Sol multi-missions dALTimetrie, d'orbitographie et
228 de localisation précise / Data Unification and Altimeter Combination System) system
229 (Pujol et al., 2016), distributed through the Copernicus Marine and Environment
230 Monitoring Service

231 (<http://marine.copernicus.eu/documents/QUID/CMEMS-SL-QUID-008-032-051.pdf>).

232 The data were analysed from 1 July 2014 to 1 July 2018. We used the gridded surface
233 geostrophic velocity anomalies derived from the Sea Level Anomaly gradients to
234 calculate the Eddy Kinetic Energy (EKE), as one half of the sum of the squared eddy
235 velocity components.

236 Surface wind stress data were extracted from the European Centre for
237 Medium-Range Weather Forecasts reanalysis, ERA5
238 (<https://www.ecmwf.int/en/forecasts/datasets/reanalysis-datasets/era5>). ERA5 has a
239 horizontal resolution of 30 km and provides hourly estimates of atmospheric, land and

240 oceanic climate variables. In this study, we use 6h-output covering July 2014 to July
241 2018.

242 Daily time-series of horizontal velocity from the GLORYS12V1 product are
243 extracted at the location of ADCP1. GLORYS12V1 is the Copernicus Marine and
244 Environment Monitoring Service global ocean eddy-resolving reanalysis covering the
245 altimetry era from 1993 (1/12° horizontal resolution and 50 vertical levels,
246 <http://resources.marine.copernicus.eu/documents/PUM/CMEMS-GLO-PUM-001-030.pdf>
247 [f](#)). The model component is the NEMO platform driven at the surface by European
248 Centre for Medium-Range Weather Forecasts ERA-Interim reanalysis.

249 Climatological upper-ocean temperature and salinity were extracted from the
250 Monthly Isopycnal / Mixed-layer Ocean Climatology, MIMOC (Schmidtko et al., 2013).
251 MIMOC has a 0.5° lateral resolution and 81 standard pressure levels between 0-
252 1950 dbar.

253

254 3. Transport Calculation

255 The total transport (T_{TOT}) through the Rockall Trough is calculated as the sum of
256 the transport in the western wedge (T_{WW}), the mid-basin (T_{MB}), and the eastern wedge
257 (T_{EW}) (Eq.1, Figure2a).

$$\begin{aligned}
 T_{TOT} &= \iint_{RT \text{ section}} v(x, z) dx dz \\
 258 \quad &= \iint_{WW} v dx dz + \iint_{MB} v dx dz + \iint_{EW} v dx dz \quad (\text{Eq. 1}) \\
 259 \quad &= T_{WW} \quad + \quad T_{MB} \quad + \quad T_{EW}
 \end{aligned}$$

260

261 Mid-basin transport is estimated from dynamic height moorings WB1 and WB2 in
262 the west, and EB1 in the east. Transport in the western wedge is calculated from
263 current meter data from mooring WB1. Eastern wedge transport is calculated from
264 current meter data from the EB1 and ADCP1 moorings and ocean reanalysis. In

265 addition, the meridional wind-driven Ekman transport is computed as a function of the
266 zonal component of the wind-stress following Gary et al. (2018).

267

268 **3.1 Mid-basin transport**

269 We compute the mid-basin geostrophic shear from the surface to the depth
270 $z_{ref} = 1760$ m. In the east, the bathymetry enables mooring EB1 to be deployed at z_{ref} .
271 However, in the west, a sedimentary body produced by the accumulation of sediment
272 under the control of bottom currents, the Feni Ridge (Figure 1b, [Howe et al., 2001]),
273 interrupts the steep bathymetry at 1600 m, with mooring WB1 placed on the top of this
274 feature. Thus, to extend the depth of the geostrophic shear calculations, we also rely on
275 mooring WB2, which is located further east at 1800 m depth. We merge the data from
276 WB1 and WB2 following the RAPID methodology to create temperature and salinity
277 profiles that extend to z_{ref} (McCarthy et al., 2015, sub-section "Design of the array"). We
278 set the location of this merged dynamic height mooring to half way between WB1 and
279 WB2.

280 The mid-basin calculation requires a known velocity at one depth level. We
281 chose not to reference our mid basin geostrophic velocities to satellite altimetry because
282 of the significant uncertainty associated with the gridded Absolute Dynamic Topography
283 (ADT). By defining the uncertainty of the gridded ADT as the standard deviation of the
284 difference between the along-track and gridded ADT data, we find a mean slope error of
285 5.0 cm ($\sqrt{2.7^2 + 3.9^2}$), equivalent to a transport error of 6.8 Sv across our section
286 (Appendix A). Therefore, we use a single level of no motion. Previous work set a
287 constant level of no motion across the Rockall Trough (Ellett & Martin, 1973; Holliday et
288 al., 2000, 2015). However, the mooring array shows barotropic flow at both the eastern
289 and western boundaries, so we use the deepest depth level of the dynamic height
290 moorings (z_{ref}) as the level of no motion. This gives a basin-wide transport below
291 1250 m of approximately -0.3 Sv. The southern entrance of the Rockall Trough is the
292 only pathway deeper than 1250 m. Below this depth, the northward-flowing waters are
293 blocked by the topography (Holliday et al., 2000) and only a small net southward
294 transport of dense Wyville Thomson Overflow Water has been reported (-0.3 Sv,

295 Johnson et al., 2017). By integrating the dynamic height difference from an assumed
 296 level of no motion z_{ref} , the time-varying geostrophic velocity between the two dynamic
 297 height moorings WB and EB1, v_{MB} can be expressed as:

$$v_{MB}(z) = v(z_{ref} = 1760) - \frac{1}{f} \int_{z=1760}^z \frac{\Delta\Phi_{EB1}(z) - \Delta\Phi_{WB}(z)}{L} dz$$

298 $v_{MB}(z) = v_{ref} - v_{BC}(z)$ (Eq. 2)

299 where $\Delta\Phi$ is the dynamic height anomaly relative to z_{ref} at the western and eastern
 300 boundaries, calculated as the integral of the specific volume anomaly from z_{ref} to depth
 301 z . L is the distance between the western and eastern moorings and f is the Coriolis
 302 frequency. Following the level of no motion approximation, the reference velocity at z_{ref} ,
 303 v_{ref} , is equal to zero. The mid-basin transport T_{MB} is obtained by integrating Eq. 2 over
 304 the mid-basin area.

305

306 **3.2 Western wedge transport**

307 Transport in the western wedge is calculated by extrapolating the profile of
 308 currents measured at WB1 across the western wedge. This region, extending from
 309 13.0 °W (EEL station C) to 12.5 °W (mid-way between WB1 and WB2), is characterised
 310 by a spatially uniform mean southward current (Figure 2a). The WB1 velocities were
 311 extended eastward to 12.5 °W; whilst west of WB1, velocities were linearly interpolated
 312 between those at WB1 to zero, either at the eastern boundary of the wedge (13.0 °W) or
 313 the seabed if this was intercepted. On Rockall Bank (between 13.5 °W and 12.9 °W),
 314 the mean velocities from 11 LADCP sections show evidence of a northward jet
 315 (Figure 2a) in the upper 250 m, also indicated by a V-shape in the isopycnals. This
 316 small northward flow seems to recirculate around Rockall Bank and therefore is
 317 excluded from our calculation. Instead, the upper 250 m of the western wedge is filled
 318 by linearly interpolating velocities from WB1 to zero at 12.9 °W, instead of 13.0 °W.

319

320 **3.3 Eastern wedge transport**

321 It was planned that the transport in the eastern wedge would be calculated using
322 velocities measured at EB1 and ADCP1. However, due to repeated losses of ADCP1,
323 we used the GLORYS12v1 ocean reanalysis to recreate velocity time-series at the
324 location of ADCP1. The time-series of ADCP1 depth-average meridional velocity
325 compare well with GLORYS during the 8-month period of available observations
326 ($r = 0.5$, p -value = 0.07, Figure S2). As the mean difference between the observations
327 and reanalysis is 7.6 cm/s (standard deviation of 8.9 cm/s), the GLORYS velocity
328 time-series was offset by 7.6 cm/s in order to have the same mean velocity as the
329 ADCP1 deployment (Figure S2). The eastern wedge above 750 m is filled by linearly
330 interpolating the velocities from the EB1 mooring (9.6 °W) and GLORYS-ADCP (the
331 time-series of adjusted velocities extracted from GLORYS at the ADCP1 location at
332 9.3 °W). East of ADCP1, the eastern wedge is filled with velocities from
333 GLORYS-ADCP by linearly decreasing them to zero at the edge of the continental shelf
334 (9.2 °W). The transport below 750 m is calculated by uniformly extrapolating the vertical
335 profile of velocity at EB1 to the eastern wedge area. From 2020, gliders are deployed in
336 the shelf edge current to provide continuous observations between the 200m contour
337 and EB1 mooring.

338

339 **4 Accuracy of the estimated transport**

340 The accuracy of the estimated transports is impacted by two types of error:
341 instrumental and methodological (surface extrapolation of mooring data, vertical
342 gridding, and horizontal interpolation of the flow field in the boundary currents). Our aim
343 is to provide a realistic estimate of errors associated with each of these sources, and
344 their net impact on the total flux. In this section we briefly describe the methods and
345 results, with a more detailed description given in Text S1. Instrumental errors were
346 evaluated by error propagation using the pressure, temperature, salinity and velocity
347 accuracies provided by the instrument manufacturers. We evaluate methodological
348 errors using repeat LADCP and CTD data from EEL hydrographic sections and a
349 seasonal climatology of temperature and salinity. We calculate the transports in the

350 boundaries and mid-basin using the full horizontal and vertical resolution of the
351 LADCP/CTD data (method M1) and using a subsampled version of the same dataset
352 (method M2). Method M2 simulates the discrete measurement levels of the moored
353 instruments and reproduces the method used to calculate the mooring array transport
354 (as described in section 3). The mean bias error and RMS (root mean square) error for
355 each region (western wedge, mid-basin and eastern wedge) are defined as the mean of
356 the differences in transport between methods M2 and M1, and the standard deviation of
357 the transport differences respectively. The mean bias error for the section as a whole is
358 calculated as the sum of the regional bias errors, whilst the total RMS error is defined as
359 the square root of the sum of the squared regional RMS errors.

360 An overall estimate of the error for the total Rockall Trough transport is given by
361 combining the errors associated with the gridding, calibration and vertical extrapolation
362 of the mid-basin dynamic height moorings, with the errors in the western wedge
363 (horizontal extrapolation and instrument accuracy) and eastern wedge (horizontal
364 extrapolation and use of ocean reanalysis). For an optimal data return, such as in 2015-
365 2016 and 2017-2018, the RMS error is 0.93 Sv and the mean bias error 0.03 Sv.
366 However, instrument failure or losses impact both types of error. For example, in 2014-
367 2015 when the CTD at 1000 m on EB1 failed, the RMS error was 1.10 Sv and the mean
368 bias error -0.39 Sv. Similar errors were obtained in 2016-2017 when a CTD deployed at
369 250 m on EB1 was lost (Table S1).

370

371 **5 Results**

372 **5.1 Circulation and transport variability**

373 **5.1.1 Mean circulation features**

374 The mean cross-section velocity from EEL LADCP data (1996-2017) shows i) a
375 southward flow in the western wedge, ii) a northward flow between Rockall Bank and
376 the Anton Dohrn seamount superimposed onto an anticyclonic recirculation around the
377 seamount, and iii) a northward flow at the eastern boundary along the continental shelf
378 associated with the shelf edge current (Figure 2a). The 2014-2018 mean of the

379 observed velocity profiles from moorings WB1, WB2, EB1 and ADCP1 (Figure 3) reflect
380 the same flow distribution across the section.

381 At WB1, there is a mean top-to-bottom southward flow of -8.0 cm/s, with a
382 maximum velocity of -10 cm/s near 1350 m corresponding to the depth of the core of
383 the Wyville Thomson Overflow Water (Johnson et al., 2017). The standard deviation
384 varies from 14.5 cm/s at 100 m depth to 5.8 cm/s at 1420 m depth. At WB2, the
385 mean \pm one standard deviation is 0.3 ± 4.0 cm/s highlighting the eastern limit of this
386 top-to-bottom mean southward flow found in the western wedge.

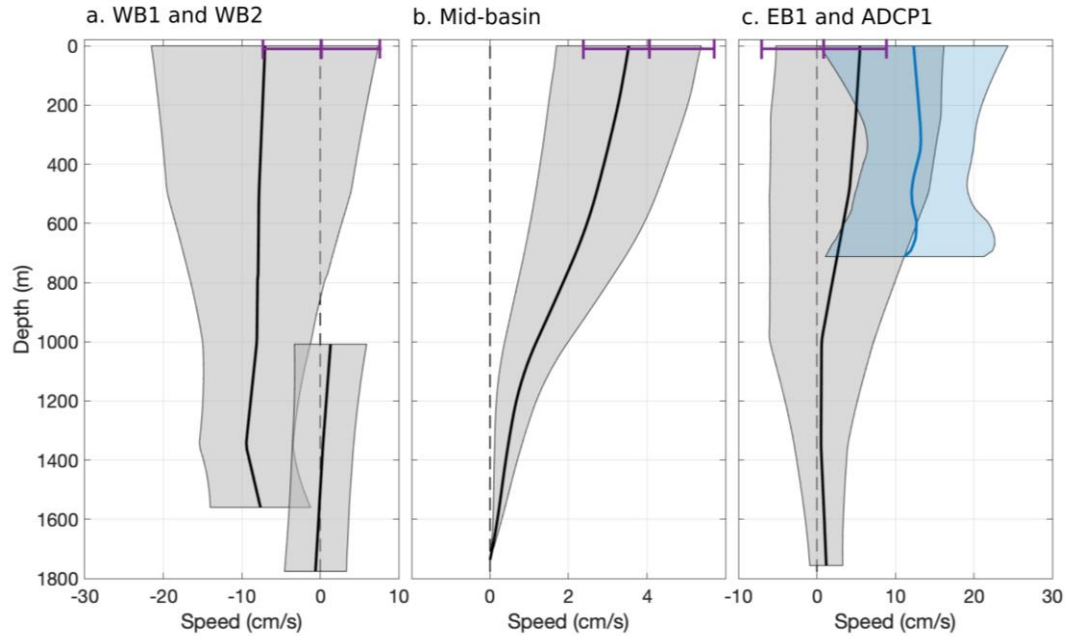
387 In the mid-basin, the mean geostrophic current is northward (vertical average of
388 1.7 cm/s) and surface intensified: the mean current at 100 m depth is 3.5 ± 1.8 cm/s.

389 At EB1, the current varies from 5.5 ± 10.7 cm/s near the surface to 1.2 ± 2.1 cm/s
390 at 1760 m depth, with a vertical average of 2.5 cm/s. Over the continental slope, the
391 8-month record from ADCP1 (Nov. 2014 – Jun. 2015) indicates a mean northward flow
392 which is relatively homogenous with depth. The vertical average of the mean northward
393 current is 12.6 cm/s and the standard deviation is 0.4 cm/s.

394 In the mid-basin and the eastern wedge, most of the northward flow is found in
395 the upper 1000 m.

396

397



398

399 Figure 3: Four-year mean (\pm one standard deviation) of the 25-day low-pass northward
 400 currents for (a) WB1 and WB2, (b) the dynamic height moorings and (c) EB1 with
 401 ADCP1. The 8-month mean northward current from ADCP1 is indicated in blue (Nov.
 402 2014 – Jun. 2015). The horizontal purple line in each panel indicates the mean \pm one
 403 standard deviation of the northward surface absolute geostrophic current from altimetry
 404 (L4 gridded product), calculated over the same time-period (Text S2).

405

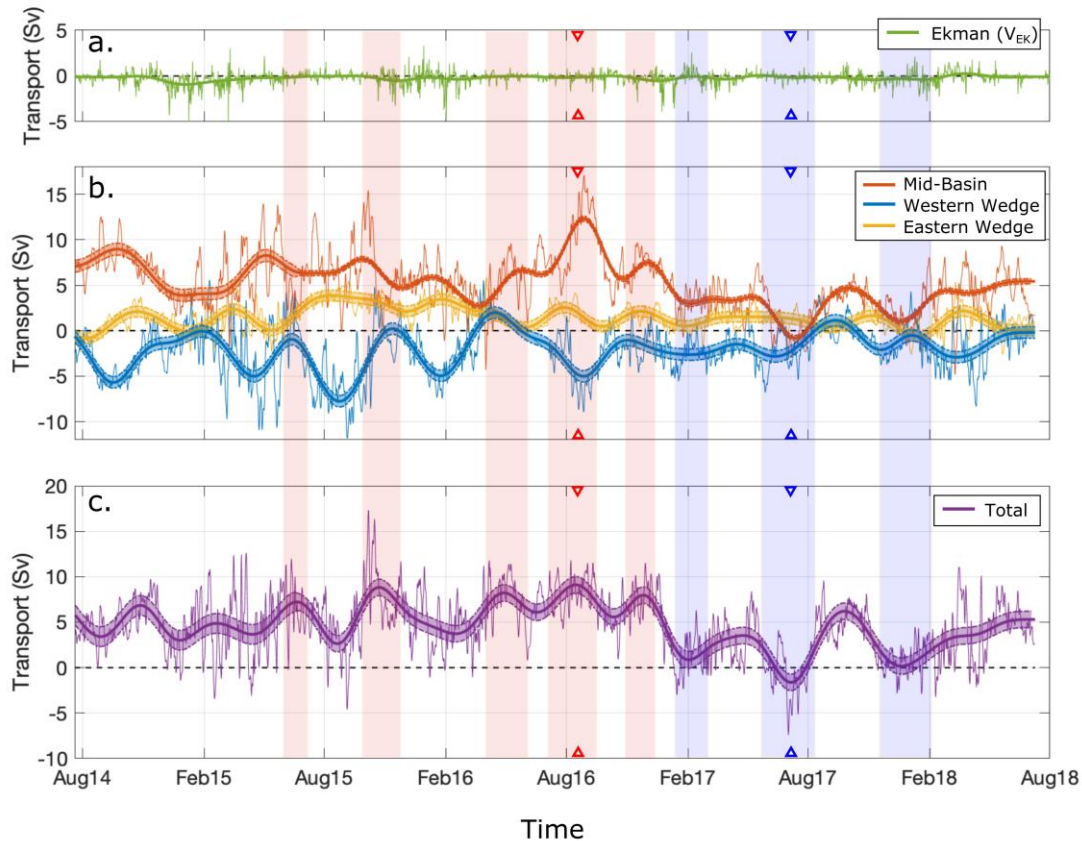
406 5.1.2 Mean transports and variability

407 A surprising feature revealed by the Rockall Trough mooring array is the large
 408 range of the total transport (24.7 Sv), spanning from -7.4 Sv to 17.3 Sv in the 40h
 409 low-pass filtered time-series. The total transport variability is dominated by the
 410 mid-basin and western wedge transport time-series (Figure 4). To focus attention on
 411 sub-annual and inter-annual time-scales, we used a third-order Butterworth filter with a
 412 cutoff period of 90 days to filter the transport time-series following (Bower & von Appen
 413 2008). For the rest of this study, we focus on the 90-day low-pass filtered transport
 414 time-series, which spans from -1.6 Sv to 9.1 Sv (10.7 Sv).

415 The total transport across the section is mainly northward, with a
 416 mean \pm one standard deviation of 4.5 ± 2.3 Sv and a standard error on the mean (SE)
 417 of 0.8 Sv. The Ekman transport calculated along the section varies from -0.93 Sv to
 418 0.25 Sv, with a mean \pm one standard deviation of -0.20 ± 0.21 Sv. This is an order of

419 magnitude smaller than the total transport (Figure 4a), and therefore the Ekman
 420 transport is considered as a negligible contribution to the net meridional transport and is
 421 not included.

422 On average, the flow is southward in the western wedge (-2.0 ± 1.9 Sv, SE:
 423 0.4 Sv), northward in the mid-basin (5.2 ± 2.4 Sv, SE: 0.7 Sv) and northward in the
 424 eastern wedge (1.4 ± 1.1 Sv, SE: 0.3 Sv) (Figure 4b,4c, Table 1).



425
 426 Figure 4: Time-series of 40-hour (thin lines) and 90-day (thick lines) low-pass filtered
 427 transport for: (a) the meridional component of the Ekman transport, (b) the eastern
 428 wedge, western wedge and mid-basin, and (c) for the whole section. Shaded areas
 429 correspond to the accuracy of the different time-series (\pm one RMS error, see section 4
 430 for more details). Extrema in transport are indicated by triangle markers on top of the
 431 subpanels (the maximum on 15 August 2016 is in red, and the minimum on 06 July
 432 2017 is in blue). The blue/red shaded areas indicate periods of low/high transport,
 433 defined as when the total transport is inferior/superior to the mean
 434 transport \pm one standard deviation.

435

436 The transport maximum in the Rockall Trough is in August 2016 (9.1 Sv), due to
437 an extreme northward transport in the mid-basin (12.3 Sv) (Figure 4b, Figure S3). The
438 total transport minimum is in July 2017 (-1.6 Sv), associated with the lowest mid-basin
439 transport recorded during the 4-years of measurement (-0.8 Sv, Figure 4b, Figure S3).

440 In order to characterize the vertical and horizontal structure of the transport
441 during periods of high or low northward transport in the Rockall Trough, we define two
442 composites-states. For the high transport composite, we average together all the
443 periods when the total transport was greater than the mean plus one standard deviation
444 (red shaded areas on Figure 4). For the low transport composite, we average together
445 all the periods where the total transport was lower than the mean minus one standard
446 deviation (blue shaded areas on Figure 4). Each composite-period represents 15% of
447 the 4-year record. The total transport (mean \pm one standard deviation) is 7.8 ± 1.0 Sv
448 for the high transport period and 0.6 ± 0.6 Sv for the low transport composite (Table 1).
449 The high transport composite is associated with a higher northward transport in the
450 mid-basin (7.3 Sv) and in the eastern wedge (2.0 Sv), as seen on Figure 5. The low
451 transport state is associated with a weaker northward transport in the mid-basin (1.8 Sv)
452 and in the eastern wedge (0.6 Sv). The western wedge transport (mean \pm one standard
453 deviation) is not different during the periods of high and low transport, -1.5 ± 0.7 Sv
454 and -1.8 ± 0.3 Sv respectively.

455

456

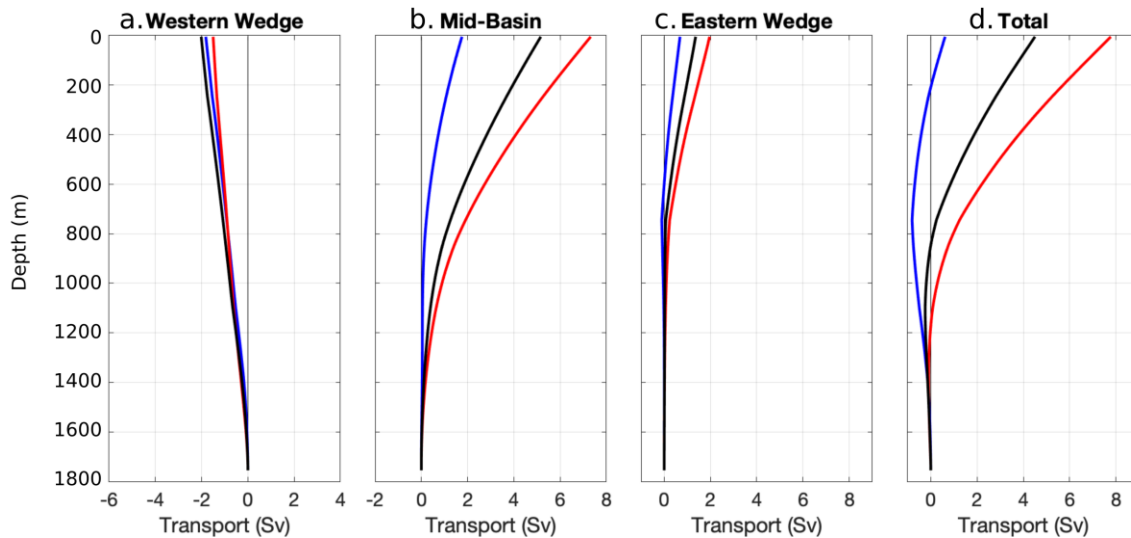
457 Table 1: Statistics of the 90-day low-pass filtered transport time-series for the
 458 2014-2018 period: SD: standard deviation, SE: Standard error; ITS: Integral Time Scale
 459 (measure of the correlation length), EDOF: Effective Degree Of Freedom calculated
 460 from the ITS (for 90-day low-pass filtered time-series). ITS is calculated as twice the
 461 area of the positive autocorrelation function from zero to the first zero crossing. Mean
 462 and standard deviation for the high [HI] and low [LO] transport-composite states are
 463 also indicated.

464

| | Mean | SD | SE | Min | Max | Range | ITS | EDOF | [HI] | | [LO] | |
|--------------|------------|------------|------------|-------------|------------|-------------|--------------|------------|------------|------------|------------|------------|
| | (Sv) | (Sv) | (Sv) | (Sv) | (Sv) | (Sv) | (days) | | Mean | SD | Mean | SD |
| | (Sv) | (Sv) | (Sv) | (Sv) | (Sv) | (Sv) | (days) | | (Sv) | (Sv) | (Sv) | (Sv) |
| Total | 4.5 | 2.3 | 0.8 | -1.6 | 9.1 | 10.7 | 150.1 | 9.7 | 7.8 | 1.0 | 0.6 | 0.6 |
| WW | -2.0 | 1.9 | 0.4 | -7.8 | 2.0 | 9.8 | 61.6 | 24.4 | -1.5 | 0.7 | -1.8 | 0.3 |
| MB | 5.2 | 2.4 | 0.7 | -0.8 | 12.3 | 13.1 | 138.1 | 10.5 | 7.3 | 0.7 | 1.8 | 0.4 |
| EW | 1.4 | 1.1 | 0.3 | -0.9 | 3.9 | 4.8 | 146.7 | 10.2 | 2.0 | 0.3 | 0.6 | 0.2 |

465

466



467

468 Figure 5: Cumulative transport integrated from 1760 m to the surface for: (a) the
 469 western wedge, (b) the mid-basin, (c) the eastern wedge and (d) the whole section. The
 470 black line corresponds to the 4-year mean, whilst the coloured lines show the mean for
 471 the period of low transport (inferior to the mean - one standard deviation, blue) and the
 472 period of high transport (superior to the mean + one standard deviation, red).
 473 Cumulative transport at the time of the maximum and minimum Rockall Trough
 474 transports are shown on Figure S3.

475

476 **5.1.3 Trends and Seasonal Cycles**

477 For the 2014-2018 period, the mid-basin component has a significant downward
478 trend in transport of -1.0 Sv/year (95% confidence interval of [-2.0,0.0] Sv/year, see
479 Table 2), explaining 23% of the variance in the transport time-series. No significant
480 downward linear trends (both lower and upper limits of the 95% confidence interval are
481 negative) were detected in the western or eastern wedge transport time-series.

482 Seasonal cycles were calculated for each component of the array as the monthly
483 average of the detrended time-series. The ranges of the seasonal cycle are 2.4 Sv in
484 the western wedge, 3.5 Sv in the mid-basin and 1.2 Sv in the eastern wedge (Table 2)
485 and account for, respectively, 24%, 27%, and 25% of the range of variability observed in
486 the 90-day low-pass filtered time-series (Table 1).. The seasonal cycles have two
487 maxima found during fall (Sep.-Dec.) and spring (Mar.-May) and two minima found in
488 winter (Jan.-Feb.) and in summer (Jun.-Aug) (Figure 6, Table 2).

489 The standard error of the monthly seasonal mean is maximum at the end of the
490 summer (August-September); it varies from 0.1 Sv (March) to 0.5 Sv (September) for
491 the total transport time-series, 0.1 Sv (July) to 0.6 Sv (September) for the western
492 wedge, 0.1 Sv (October) to 0.4 Sv (August) for the mid-basin, and 0.0 Sv (November) to
493 0.3 Sv (August) for the eastern wedge.

494

495

496

497 Table 2: Trend and seasonal cycle extrema for the observed transport time-series
 498 (90-day low-pass filtered) calculated for the total transport time-series (TOT), the
 499 western wedge (WW), the mid-basin (MB) and the Eastern Wedge (EW). The standard
 500 error (SE) is calculated for each month as the monthly standard deviation divided by the
 501 square root of the degree of freedom.

502

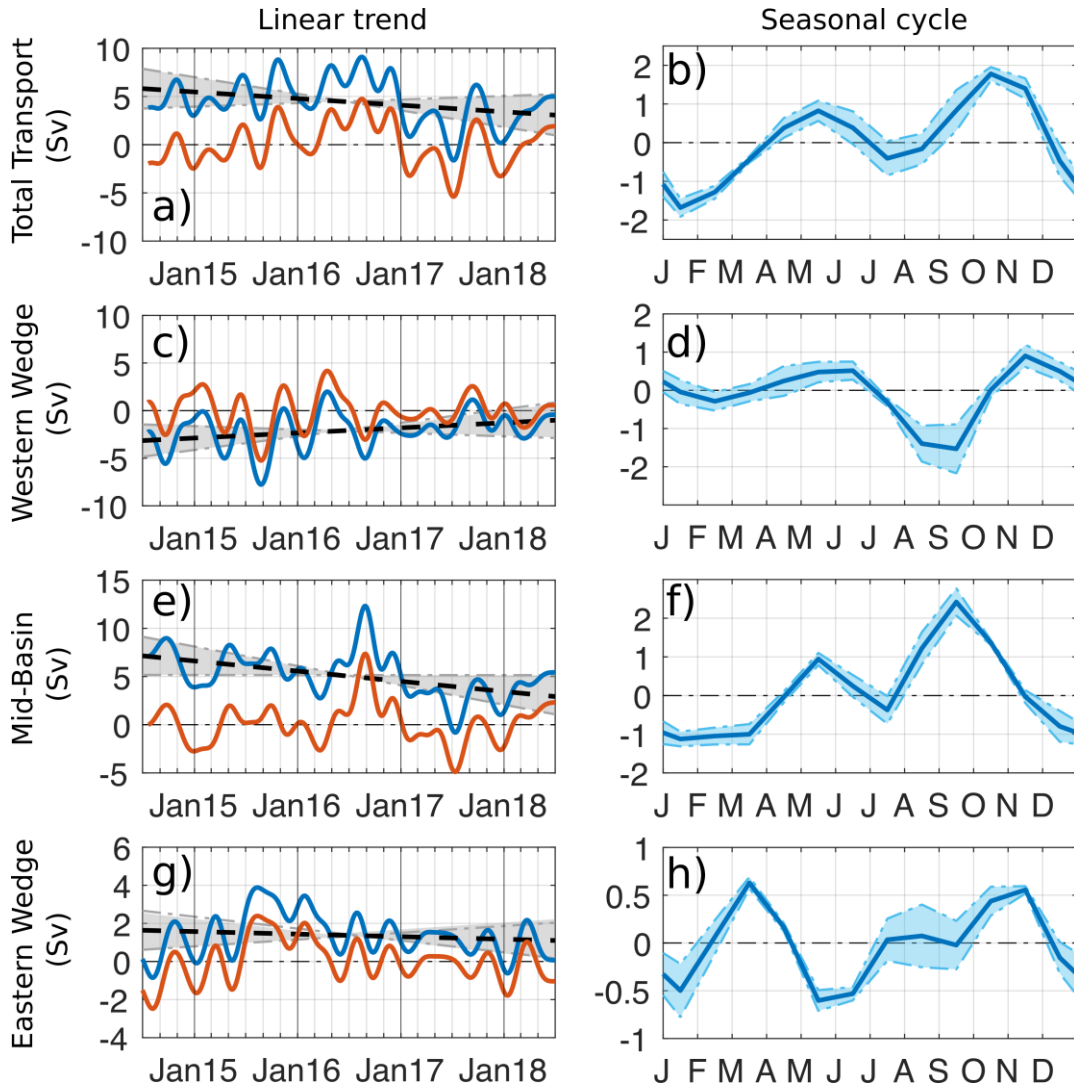
| | Trend | | | Seasonal cycle | | | | | | | | | | | | |
|-----|---------|----------------|---------------|----------------|-----------------|------|-----|-----------------|------|-----|-------------------|------|-----|-------------------|------|-----|
| | | | | Range | Primary maximum | | | Primary minimum | | | Secondary maximum | | | Secondary minimum | | |
| | Trend | R ² | 95% CI | | [Sv] | Max | SE | Month | Min | SE | Month | Max | SE | Month | Min | SE |
| | [Sv/yr] | | [Sv/yr] | | [Sv] | [Sv] | | [Sv] | [Sv] | | [Sv] | [Sv] | | [Sv] | [Sv] | |
| TOT | -0.7 | 0.11 | [-1.7 0.4] | 3.4 | 1.8 | 0.2 | Oct | -1.7 | 0.2 | Jan | 0.8 | 0.3 | May | -0.4 | 0.4 | Jul |
| WW | 0.5 | 0.11 | [-0.3 1.4] | 2.4 | 0.9 | 0.3 | Nov | -1.5 | 0.6 | Sep | 0.5 | 0.2 | Jun | 0.1 | 0.3 | Dec |
| MB | -1.0 | 0.23 | [-2.0 0.0] | 3.5 | 2.4 | 0.4 | Sep | -1.1 | 0.2 | Jan | 0.9 | 0.2 | May | -0.4 | 0.4 | Jul |
| EW | -0.1 | 0.02 | [-0.7 0.4] | 1.2 | 0.6 | 0.1 | Mar | -0.6 | 0.1 | May | 0.5 | 0.1 | Nov | -0.0 | 0.2 | Sep |

503

504

505

506



507

508 Figure 6: Linear trend (a, c, e, g) and seasonal cycle (b, d, f, h) for the total, western
 509 wedge, mid-basin and eastern wedge transports. In the left subpanels, trends (black
 510 dashed lines) are calculated by fitting a line to the transport time-series (blue lines), the
 511 grey shaded area represents the 95% confidence intervals for the linear trend.
 512 Detrended time-series are plotted in orange. Trends and confidence intervals are
 513 indicated in Table 2. Seasonal cycles calculated as the monthly average of the
 514 detrended data are shown in the right subpanels. The light blue shaded area shows the
 515 monthly mean \pm one standard error (standard deviation divided by the square root of the
 516 degree of freedom).

517

518

519

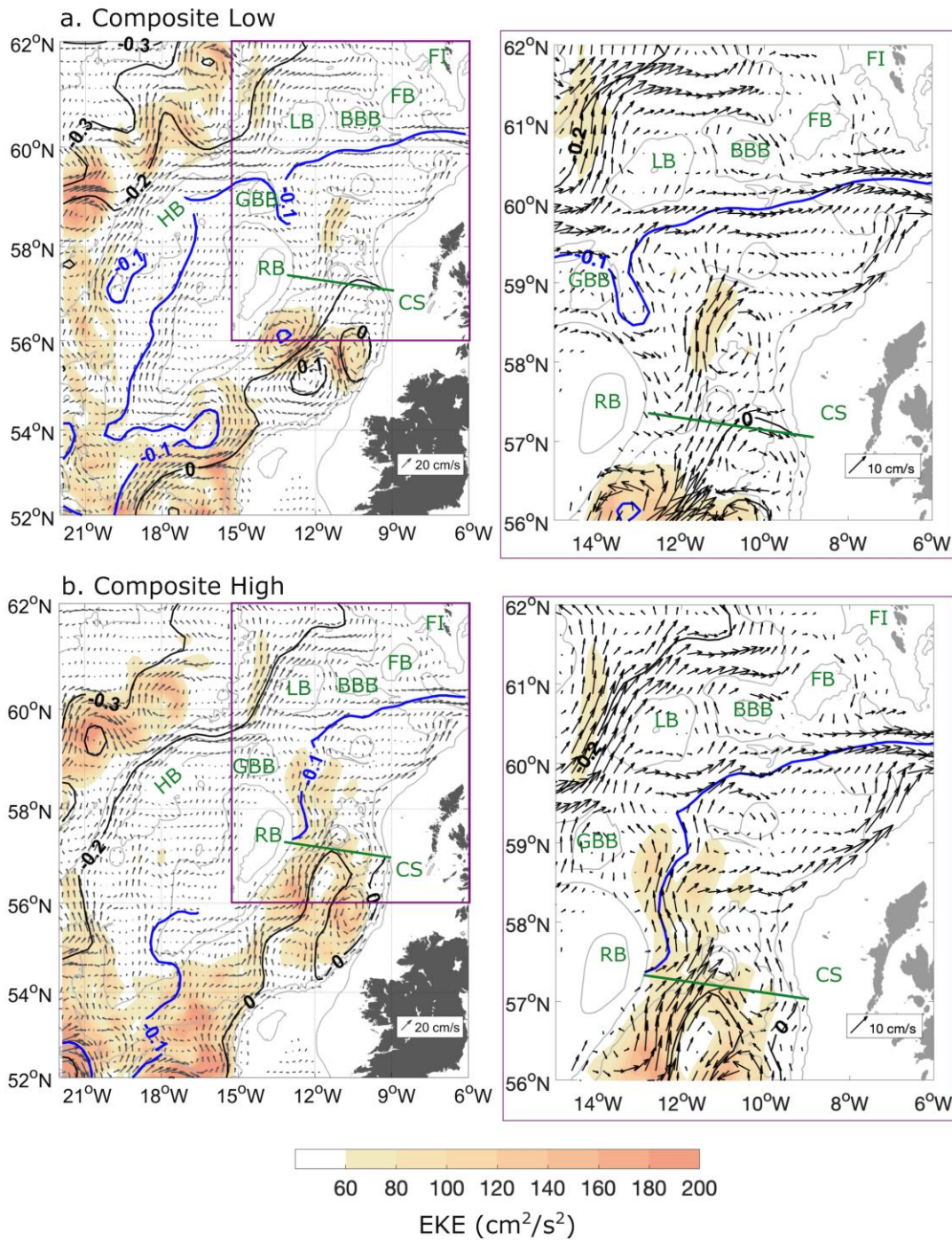
520 **5.2 Large-scale circulation changes associated with high and low transport** 521 **regimes**

522 The mesoscale variability in the subpolar North Atlantic and the intensity of the
523 eddy activity represented by the EKE has been documented in several studies. At
524 midlatitudes away from topography, and particularly in the North Atlantic, areas of high
525 EKE are associated with energetic currents. Therefore, changes in the patterns of EKE
526 can be indicative of changes in the strong current systems (Chafik et al., 2014;
527 Heywood et al., 1994; Reverdin et al., 2003; Volkov, 2005). Using surface EKE
528 computed from satellite altimetry between 2014 and 2018, we consider whether there
529 are characteristic spatial patterns of EKE associated with the high and low transport
530 states defined by the mooring data.

531 The 90-day low-pass filtered EKE fields, absolute surface geostrophic currents
532 and ADT are shown in Figure 7 for periods of low and high transport (snapshots at
533 transport minimum and maximum in July 2017 and August 2016 respectively are shown
534 on Figure S4). EKE reaches $200 \text{ cm}^2/\text{s}^2$ in the Rockall Trough in both composite-states
535 (Figure 7). During the low-transport period, EKE is organized around eddy-like
536 structures centred on 12°W , 56°N . During the high-transport period a strong NAC jet,
537 characterised by an elevated EKE-band, stretches from the entrance of the Rockall
538 Trough to north of the array ($\sim 59^\circ\text{N}$).

539 During periods of low transport, there is a westward shift of the -0.1m ADT
540 contour (Figure 7a). In contrast, during the high-transport period and the 2014-2018
541 period, the mean -0.1m contour is located east of Rockall Bank in the Rockall Trough
542 (Figure 7b). We note that when considering the 2014-2018 mean, the -0.1 m contour is
543 similarly located (Figure S1). However, the location of the 0 m ADT contour is similar
544 during both the high and low transport times, meaning that the zonal gradient of ADT in
545 the Rockall Trough is reduced during the period of low transport and increased for
546 periods of high transport. This agrees well with the reduction of the mid-basin
547 geostrophic transport observed during the low-transport period (Figure 4b). The
548 westward shift of the -0.1m contour is even larger at the time of the Rockall Trough
549 transport minimum (Jul. 2017, Figure S4), when it reached 20°W in the Iceland Basin.

550 Other regional circulation changes occur during the low transport periods, such
551 as the retroflexion of the NAC at the entrance of the Trough (Figure 7a and
552 Figure S4a), and the presence of an eastward flow between George Bligh Bank and
553 Lousy Bank (60 °N, 13.5 °W). In contrast, during the high transport period, the NAC can
554 be distinguished as a continuous flow into the Rockall Trough along 12 °W-13 °W.
555 During the period of high-transport (Figure 7b, Figure S4b) and on the 4-year mean map
556 (Figure S1), the NAC appears to separate into several eastward-propagating
557 sub-branches. These eastward flows can be seen south and north of the Anton Dohrn
558 seamount (57 °N and 58.5 °N) and south of Bill Bailey Bank (60 °N). During the
559 high-transport period, an additional NAC sub-branch can be seen flowing northward
560 between Lousy Bank and Bill Bailey Bank (Figure 7b).
561



562

563 Figure 7: 90-day low-pass filtered EKE (color scale) and surface absolute geostrophic
 564 currents (black arrows) for the composite-periods of: (a) low and (b) high transports.
 565 Data are plotted for water depths greater than 400 m and velocities exceeding 2.5 cm/s.
 566 The green line near 57.5°N indicates the Rockall Trough mooring array. Mean absolute
 567 dynamic topography contours are plotted as thick black lines with a contour interval of
 568 0.1 m, with the -0.1 m contour in blue. Bathymetry from ETOPO are shown in grey for
 569 the 200, 1000, 2000, and 3000-m contours. Acronyms: eddy kinetic energy (EKE); Earth

570 TOPOgraphic database (ETOPO); other acronyms defined in Figure 1. EKE and
571 surface absolute geostrophic current at the time of the minimum and maximum
572 transport are shown in supplementary material (Figure S4).
573

574

575 **6 Discussion**

576 From four years of UK-OSNAP mooring data we have quantified and described
577 the variability of the Rockall Trough transport, giving the first continuous multi-year
578 measurements. The west and east boundary currents are measured directly using
579 current meters, while the CTDs on moorings WB1/2 and EB1 are used to compute
580 dynamic height profiles in order to calculate the mid-basin geostrophic transport. We
581 show that the design of the mooring array is fit for purpose; methodological and
582 instrumental errors give a mean bias error of 0.03 Sv and a root mean square error of
583 0.93 Sv on a mean total transport of 4.5 Sv.

584 There is an observing gap in the shelf edge current (east of 9.6°W); the
585 bottom-mounted ADCP within a trawl-resistant frame suffered heavy fishing-related
586 damage on multiple deployments. Due to repeated instrument losses, we used
587 GLORYS12v1 (1/12° global ocean reanalysis) to recreate velocity time-series at the
588 location of the ADCP mooring. The reanalysis was able to reproduce the correct vertical
589 structure of the 4-year mean current profiles at the mooring sites but had a bias
590 of -7.6 cm/s compared to the mean velocity of a successful 8-month ADCP deployment
591 which we accounted for. The error of the model-based reconstruction of the shelf edge
592 current transport was assessed by applying the same methodology on repeated EEL
593 LADCP sections and comparing it to the actual LADCP velocity field. We note that the
594 uncertainty associated with our method for estimating the shelf edge current (mean bias
595 error of 0.2 Sv and RMS error of 0.6 Sv, Table S1) is small compared to the transport
596 and variability in the mid-basin and in the western Rockall Trough. A new observing
597 strategy has been adopted from 2020 onwards, replacing the ADCP mooring with a
598 repeated glider survey.

599 Our new transport estimates agree with previously published work. Although we
600 used a slightly different methodology, the mean for the first 21 months (5.1 Sv) closely
601 matches the NAC transport in the Rockall Trough calculated by Lozier et al. (2019):
602 5.2 Sv flowing east of 13.0 °W for the layer $\sigma_0 < 27.66 \text{ kg/m}^3$. The 4-year mean total
603 meridional transport measured in the Rockall Trough (4.5 Sv, standard error of 0.8 Sv)

604 is in the range of previous EEL hydrographic estimates: 3.7 ± 2.4 Sv for 1975-1998
605 (Holliday et al., 2000) and 3.0 ± 3.7 Sv for 1997-2014 (Holliday et al., 2015). However,
606 these previous estimates used a mid-depth level of no motion, and our new direct
607 current measurements in the boundaries show significant barotropic flows, particularly
608 east of the Rockall Bank where a 4-year mean southward flow of -2.0 Sv was observed.
609 Similar barotropic and bathymetrically steered flows have been observed further west
610 from repeated glider observations, on the western and eastern flanks of the Rockall
611 Hatton Basin (Houpert et al., 2018). Work is ongoing to quantify the barotropic
612 component of the flow between Iceland and Scotland by revisiting historical
613 hydrographic sections and referencing the geostrophic shear to direct current
614 measurements from ship-mounted ADCP and LADCP.

615 A new result from the Rockall Trough mooring array is the strong intra-annual
616 and seasonal variability in the total transport. The 90-day low-pass filtered transport
617 time-series has a range of 10.7 Sv, varying from 9.1 Sv in August 2016 to -1.6 Sv in
618 July 2017. The continuous observations allow us to calculate the seasonal cycle of the
619 Rockall Trough transport. With an amplitude of 3.6 Sv during the 2014-2018 period, the
620 seasonal cycle of the Rockall Trough transport accounts for 33% of the range of
621 variability observed in the 90-day low-pass filtered time-series. This estimate is three
622 times higher than that found from hydrographic data by Gary et al. (2018), albeit with
623 the same periods for the transport extrema (maximum in spring and fall; minimum in
624 summer and winter). As mentioned by Gary et al. (2018), their seasonal cycle is partly
625 masked by mesoscale eddies, interannual variability and observational aliasing, which
626 can explain the amplitude difference with our estimate.

627 A key finding is the occurrence of states of high and low transport in the Rockall
628 Trough which appear to be related to changes in the NAC circulation. During the high
629 transport state, the total transport is 7.8 ± 1.0 Sv and during the low transport state the
630 total transport is 0.6 ± 0.6 Sv, with associated changes in the mid-basin geostrophic
631 transport. During the low-transport period, the western wedge transport (-1.8 Sv)
632 entirely compensates the mid-basin geostrophic transport (1.8 Sv) and the net transport
633 reflects the eastern wedge transport. During the low-transport state, EKE is organized
634 around eddy-like structures while during the high-transport state, a strong NAC jet,

635 characterised by an elevated EKE-band, stretches from the entrance of the basin to
636 north of the array. We identified other regional circulation changes associated with the
637 low-transport state, including the retroflexion of the NAC at the entrance of the Trough,
638 and the presence of an eastward flow between George Bligh Bank and Lousy Bank. A
639 similar shift between two states of variability was found in the Iceland Basin by Zhao et
640 al. (2018). They found that alternating eddy and front patterns in the eastern Iceland
641 Basin contribute significantly to the total poleward heat transport variability on time
642 scales from sub-seasonal to interannual. Chafik et al. (2014) found that sea surface
643 height (SSH) slopes from satellite altimetry vary out of phase west and east of the
644 Hatton Bank: a decrease in the SSH slope west of the Hatton Bank appears to be
645 compensated by an increase of the SSH slope east of the Hatton Bank, and *vice versa*.
646 More studies are needed to quantify the relationship between the NAC variability
647 between the Iceland Basin and the Rockall Trough (e.g. are the high-transport states in
648 the Rockall Trough associated with low-transport states in the Iceland Basin?), and to
649 understand the nature of these “modes” of NAC variability (atmospherically-forced
650 response vs chaotic).

651 Holliday et al. (2020) reported a dramatic change in the properties of the upper
652 waters of the North Atlantic in 2014–2016, likely due to a change of the mean wind
653 stress curl pattern over the region and a much intensified subpolar gyre (Hátún &
654 Chafik, 2018). These changes in water mass properties, and an eastward shift of the
655 subpolar front, would be consistent with our findings of an increased northward
656 transport in the Rockall Trough during the 2014-2016 period. A significant decrease in
657 the mid-basin and total transport occurs between December 2016 and February 2017
658 (Figure 4). After January 2017 the mean Rockall Trough transport reduced from 5.7 Sv
659 to 2.7 Sv. The SSH gradient was reduced in the eastern subpolar North Atlantic during
660 2017, which could explain the decrease in transport observed in the Rockall Trough
661 after January 2017, however, further work is needed to better understand the links
662 between the Rockall Trough transport variability and regional circulation changes.

663 The northward transport of the NAC through the Rockall Trough (6.6 Sv) is larger
664 than previously thought and mostly takes place in the Rockall Trough interior, not via
665 the shelf edge current. Satellite altimetry shows that the mean position of the NAC

666 branch (2014-2018) is west of the Anton Dohrn Seamount between 13°W and 11°W
667 (Figure S1). This is also seen on the mean EEL LADCP section (Figure 2), where a
668 northward flow between Rockall Bank and the Anton Dohrn seamount is superimposed
669 on an anticyclonic recirculation around the seamount. Satellite altimetry also shows that
670 this main NAC branch is not completely independent of the branch flowing along the
671 shelf edge. As the mid-basin NAC branch propagates northward it seems to be “leaking”
672 water towards the east. These eastward propagating sub-branches appear to join the
673 shelf branch before it enters the Faroe-Shetland Channel (Figure S1, Figure 1). The net
674 transport across the Rockall Trough array is 2 Sv lower than the total northward
675 transport because of the presence of a southward flow east of the Rockall Bank. The
676 mechanisms driving this flow are not fully understood yet, but some evidence exists for
677 a significant recirculation of the “Icelandic” NAC branch around the Rockall Plateau
678 region (encompassing the Hatton Bank, Hatton-Rockall Basin and Rockall Bank). For
679 example, Gary et al. (2018) used the time-mean barotropic streamfunction from the
680 ocean model VIKING20 and showed that a 2 Sv anticyclonic recirculation exists around
681 the Rockall Plateau. Howe et al. (2001) identified a zone of active seabed erosion
682 extending from George Bligh Bank to the south of Rockall Bank, between 1000m and
683 1500m depth, indicating vigorous bottom-current activity. Initially associated with the
684 Wyville Thomson Overflow Water, we think that this erosion pattern could also be the
685 imprint of the strong barotropic currents associated with the NAC recirculating around
686 the Rockall Plateau.

687 Our results, along with those of Lozier et al. (2019) contrast with a recent review
688 by Bower et al. (2019) who concluded that 90% of the total northward upper limb AMOC
689 transport was associated with the NAC in the Iceland Basin, and that the Rockall
690 Trough was a negligible pathway. This statement builds on three other studies mostly
691 based on the OVIDE oceanographic section (Daniault et al., 2016; Mercier et al., 2015;
692 Sarafanov et al., 2012). In these studies, the authors acknowledge that their studies are
693 representative of the 2002-2012 period, when the atmospheric forcing and the subpolar
694 gyre were at their weakest. Therefore, one explanation for the differences between
695 these historical and our new study could be a time-dependent partitioning of northward
696 transport between the Iceland Basin and Rockall Trough. A further explanation could be

697 the existence of subsurface pathways connecting the Iceland Basin and the Rockall
698 Trough. The presence of these pathways could explain the fate of the mean northward
699 flow of 1.8 Sv found between 650 m and 1800 m in the mid-basin. North of the mooring
700 array, the only exit pathways deeper than 650 m are the 1100 m deep channel found
701 between Rockall Bank and George Bligh Bank, and the 1200 m deep channels located
702 between George Bligh Bank, Lousy Bank and Bill Bailey Bank (Figure 1). Pollard et al.
703 (2004) showed from a survey in 1996 that 2 Sv of saline water exited the Rockall
704 Trough between Rockall Bank and Lousy Bank. Sarafanov et al., (2012) combined
705 multiple annual hydrographic measurements (2002-2008) with satellite altimetry and
706 found that 10.4 Sv is transported by the NAC across 59.5 °N between 17 °W and 4 °W,
707 in the upper-layer ($\sigma_0 < 27.55 \text{ kg/m}^3$). They found a maximum in the NAC transport
708 centred north of the Rockall Trough at 59.5 °N/14 °W, between George Bligh Bank and
709 Lousy Bank. Further work is needed to characterize and quantify the NAC pathways
710 connecting the Rockall Trough, the Iceland Basin and the Nordic Seas.

711

712 **7 Conclusions**

713 The first multi-year continuous measurements of the Rockall Trough transport
714 reveal a 4-year mean net flow of 4.5 Sv. A NAC branch in the mid-basin transports
715 5.2 Sv northward and 1.4 Sv is transported northward in the Scottish shelf edge current.
716 These pathways represent around half the net northward transport of warm water of the
717 upper-limb of the AMOC measured through the OSNAP array (Lozier et al., 2019). A
718 4-year mean southward flow of -2.0 Sv was observed in the western part of the Rockall
719 Trough, part of a wider anticyclonic recirculation around the Rockall Bank.

720 For the first time we have characterized the seasonal variability in the Rockall
721 Trough transport using 4-years of continuous measurements. The 90-day low-pass
722 filtered transport time-series has a range of 10.7 Sv, varying from 9.1 Sv in August 2016
723 to -1.6 Sv in July 2017. With an amplitude of 3.6 Sv during the 2014-2018 period, the
724 seasonal cycle of the Rockall Trough transport accounts for 32% of the range of
725 variability observed in the 90-day low-pass filtered time-series. The greatest transport is
726 found in fall (October) while the smallest is found in winter (January).

727 There is a detectable seasonal signal for the western wedge, the mid-basin,
728 eastern wedge, and the total Rockall Trough transport time-series. The seasonal cycles
729 have two maxima found during fall (Sep.-Dec.) and spring (Mar.-May) and two minima
730 found in winter (Jan.-Feb.) and in summer (Jun.-Aug) (Figure 6, Table 2).

731 A new finding is the description of two states of high and low transport in the
732 Rockall Trough which appear to be related to changes in the NAC circulation. During
733 the low-transport state, EKE is organized around eddy-like structures while during the
734 high-transport state, a strong NAC jet, characterised by an elevated EKE-band,
735 stretches from the entrance of the basin to north of the array. We also identified other
736 regional circulation changes associated with the low-transport state, including the
737 retroflexion of the NAC at the entry of the Trough, and the presence of an eastward flow
738 between George Blight Bank and Lousy Bank.

739 **8 Appendix**

740 **Appendix A: Referencing the mid-basin geostrophic shear to altimetry**

741 One possible method to estimate transport in the mid-basin is to reference the
742 geostrophic velocities to Absolute Dynamic Topography (ADT) from satellite altimetry.
743 To assess the suitability of this approach, we compared the ADT anomalies at the
744 location of moorings WB1 and EB1 to Steric Height (SH) anomalies calculated from
745 those moorings (Figure A1 a,b).

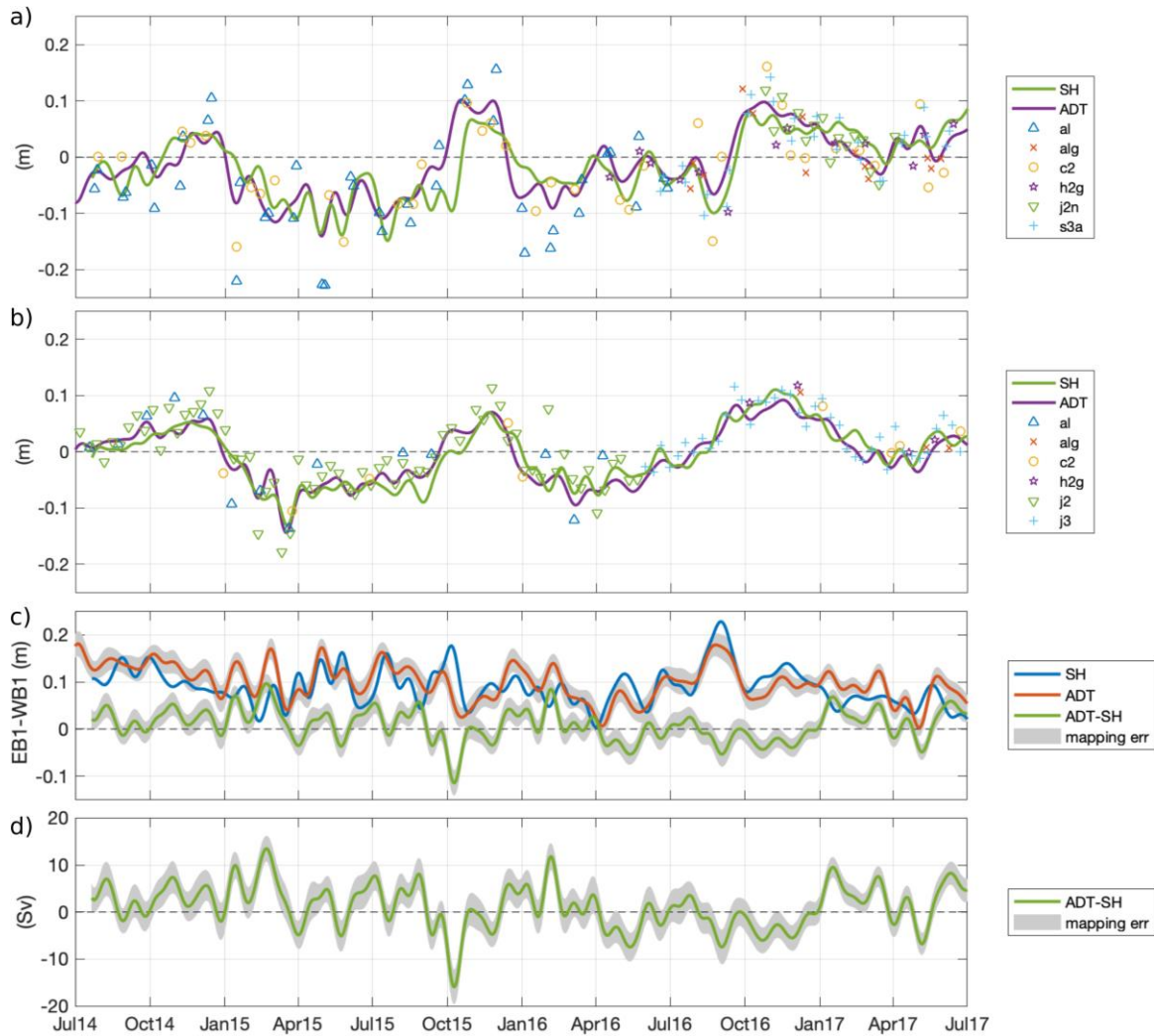
746 Although the overall agreement between the time-series of SH and gridded ADT
747 anomalies is reasonable at both locations, the mean difference is higher at WB1
748 (mean \pm standard deviation, 0.18 ± 3.56 cm) compared to EB1 (-0.02 ± 1.88 cm).
749 Additionally, several mismatches between the two time-series exist, particularly at WB1
750 (e.g. October 2015). These non-negligible differences between ADT and SH induce
751 strong transport anomalies of up to 10 Sv when the ADT is used to reference the
752 mid-basin geostrophic velocity (Figure A1 c,d).

753 To investigate possible reasons for this discrepancy, we compared the gridded ADT
754 product to the data from individual satellite tracks (Figure A1). At WB1, periods of ADT
755 and SH mismatches correspond to periods when only a few satellite tracks are close to
756 the mooring site (only Altika and Cryosat missions with a periodicity of 35 and 29 days).
757 In contrast, at EB1, which is located on the Jason track 113 (periodicity of 10 days), the
758 differences are smaller. Over the period 2014-2017, the mean \pm standard deviation of
759 the difference between the along-track and gridded ADT at the mooring locations are
760 0.6 ± 2.7 cm at EB1 and -2.3 ± 3.9 cm at WB1. This raises doubt on the quality of the
761 gridded ADT time-series at the WB1 location.

762 By defining the uncertainty of the gridded ADT as the standard deviation of the
763 difference between the along-track and gridded ADT data, we find a mean slope error of
764 5.0 cm ($\sqrt{2.7^2 + 3.9^2}$), equivalent to a transport error of 6.8 Sv.

765 The introduction of this large mean error, and the lack of a regular satellite track close to
766 WB1 before 2017, meant that we chose not to reference our mid-basin geostrophic
767 velocities to satellite altimetry.

768



769

770

771 *Figure A1: Anomaly (mean removed) of 25 day low-pass filtered Steric Height,*
 772 *calculated from 1760 m to the surface, and anomalies of Absolute Dynamic Topography*
 773 *from gridded and along-track data at (a) WB1 and (b) EB1. For each individual satellite*
 774 *track, the closest along-track data point in a radius of 15km from the mooring location is*
 775 *kept. Acronyms for satellite missions: al: Altika; alg: Altika Drifting phase; c2: Cryosat-2;*
 776 *h2g: Haiyang-2A Geodetic Phase; j2: Jason-2; j2n: Jason-2 Interleaved; j3: Jason-3;*
 777 *s3a: Sentinel-3A. ; (c) Surface slope between EB1 and WB1 due to SH, ADT and the*
 778 *difference between the two; (d) Transport between EB1 and WB1 due to the difference in*
 779 *the SH and ADT slopes.*

780

781

782 **Acknowledgments and Data Availability**

783 This analysis is a contribution to UK NERC National Capability programmes the
784 Extended Ellett Line and CLASS (NE/R015953/1), and NERC grants UK OSNAP
785 (NE/K010875/1, NE/K010875/2 ,NE/K010700/1) and UK OSNAP Decade
786 (NE/T00858X/1, NE/T008938/1). CJ has received funding from the European Union's
787 Horizon 2020 Research and Innovation Programme under grant agreement no. 678760
788 (ATLAS). This output reflects only the author's view and the European Union cannot be
789 held responsible for any use that may be made of the information contained therein.
790 This study has been conducted using E.U. Copernicus Marine Service Information.
791 BODC curates the UK-OSNAP mooring data (<http://dx.doi.org/10/c7qv>) and the
792 Extended Ellet Line dataset
793 (<https://www.bodc.ac.uk/resources/inventories/edmed/report/644/>). Please see text and
794 references for other data sources. The authors wish to thank Bee Berx and an
795 anonymous reviewer for their suggestions that have improved this manuscript.

796

797 **References**

798

- 799 Berx, B., Hansen, B., Østerhus, S., Larsen, K. M., Sherwin, T., & Jochumsen, K. (2013).
800 Combining in situ measurements and altimetry to estimate volume, heat and salt
801 transport variability through the Faroe-Shetland Channel. *Ocean Science*, *9*(4),
802 639–654. <https://doi.org/10.5194/os-9-639-2013>
- 803 Bower, A., Lozier, S., Biastoch, A., Drouin, K., Foukal, N., Furey, H., et al. (2019).
804 Lagrangian Views of the Pathways of the Atlantic Meridional Overturning
805 Circulation. *Journal of Geophysical Research: Oceans*, *124*(8), 5313–5335.
806 <https://doi.org/10.1029/2019JC015014>
- 807 Bower, A. S., & von Appen, W. J. (2008). Interannual variability in the pathways of the
808 North Atlantic Current over the mid-atlantic ridge and the impact of topography.

- 809 *Journal of Physical Oceanography*, 38(1), 104–120.
810 <https://doi.org/10.1175/2007JPO3686.1>
- 811 Chafik, L., Rossby, T., & Schrum, C. (2014). On the spatial structure and temporal
812 variability of poleward transport between Scotland and Greenland. *Journal of*
813 *Geophysical Research: Oceans*, 119(2), 824–841.
814 <https://doi.org/10.1002/2013JC009287>
- 815 Danialt, N., Mercier, H., Lherminier, P., Sarafanov, A., Falina, A., Zunino, P., et al.
816 (2016). The northern North Atlantic Ocean mean circulation in the early 21st
817 century. *Progress in Oceanography*, 146(July), 142–158.
818 <https://doi.org/10.1016/j.pocean.2016.06.007>
- 819 Egbert, G. D., & Erofeeva, S. Y. (2002). Efficient Inverse Modeling of Barotropic Ocean
820 Tides. *Journal of Atmospheric and Oceanic Technology*, 19(2), 183–204.
821 [https://doi.org/10.1175/1520-0426\(2002\)019<0183:EIMOBO>2.0.CO;2](https://doi.org/10.1175/1520-0426(2002)019<0183:EIMOBO>2.0.CO;2)
- 822 Ellett, D. J., & Martin, J. H. A. (1973). The physical and chemical oceanography of the
823 Rockall channel. *Deep-Sea Research and Oceanographic Abstracts*, 20(7), 585–
824 625. [https://doi.org/10.1016/0011-7471\(73\)90030-2](https://doi.org/10.1016/0011-7471(73)90030-2)
- 825 Gary, S. F., Cunningham, S. A., Johnson, C., Houpert, L., Holliday, N. P., Behrens, E.,
826 et al. (2018). Seasonal Cycles of Oceanic Transports in the Eastern Subpolar North
827 Atlantic. *Journal of Geophysical Research: Oceans*, 123(2), 1471–1484.
828 <https://doi.org/10.1002/2017JC013350>
- 829 Häkkinen, S., & Rhines, P. B. (2004). Decline of Subpolar North Atlantic Circulation
830 during the 1990s. *Science*, 304(5670), 555–559.
831 <https://doi.org/10.1126/science.1094917>
- 832 Hansen, B., Larsen, K. M. H., Hátún, H., Kristiansen, R., Mortensen, E., & Østerhus, S.
833 (2015). Transport of volume, heat, and salt towards the Arctic in the Faroe Current
834 1993-2013. *Ocean Science*, 11(5), 743–757. [https://doi.org/10.5194/os-11-743-](https://doi.org/10.5194/os-11-743-2015)
835 2015
- 836 Hansen, Bogi, Østerhus, S., Turrell, W. R., Jónsson, S., Valdimarsson, H., Hátún, H., &
837 Olsen, S. M. (2008). The Inflow of Atlantic Water, Heat, and Salt to the Nordic Seas

- 838 Across the Greenland–Scotland Ridge. In *Arctic–Subarctic Ocean Fluxes* (pp. 15–
839 43). Dordrecht: Springer Netherlands. https://doi.org/10.1007/978-1-4020-6774-7_2
- 840 Hátún, H., & Chafik, L. (2018). On the Recent Ambiguity of the North Atlantic Subpolar
841 Gyre Index. *Journal of Geophysical Research: Oceans*, *123*(8), 5072–5076.
842 <https://doi.org/10.1029/2018JC014101>
- 843 Hátún, Hjálmar, Sande, A. B., Drange, H., Hansen, B., & Valdimarsson, H. (2005).
844 Influence of the atlantic subpolar gyre on the thermohaline circulation. *Science*,
845 *309*(5742), 1841–1844. <https://doi.org/10.1126/science.1114777>
- 846 Heywood, K. J., McDonagh, E. L., & White, M. A. (1994). Eddy kinetic energy of the
847 North Atlantic subpolar gyre from satellite altimetry. *Journal of Geophysical
848 Research*, *99*(C11), 22525. <https://doi.org/10.1029/94jc01740>
- 849 Holliday, N. P. (2003). Air-sea interaction and circulation changes in the northeast
850 Atlantic. *Journal of Geophysical Research*, *108*(C8), 3259.
851 <https://doi.org/10.1029/2002JC001344>
- 852 Holliday, N. P., Pollard, R. T., Read, J. F., & Leach, H. (2000). Water mass properties
853 and fluxes in the Rockall Trough, 1975–1998. *Deep Sea Research Part I:
854 Oceanographic Research Papers*, *47*(7), 1303–1332.
855 [https://doi.org/10.1016/S0967-0637\(99\)00109-0](https://doi.org/10.1016/S0967-0637(99)00109-0)
- 856 Holliday, N. P., Hughes, S. L., Bacon, S., Beszczynska-Möller, A., Hansen, B., Lavín,
857 A., et al. (2008). Reversal of the 1960s to 1990s freshening trend in the northeast
858 North Atlantic and Nordic Seas. *Geophysical Research Letters*, *35*(3), L03614.
859 <https://doi.org/10.1029/2007GL032675>
- 860 Holliday, N. P., Bacon, S., Allen, J., & McDonagh, E. L. (2009). Circulation and
861 Transport in the Western Boundary Currents at Cape Farewell, Greenland. *Journal
862 of Physical Oceanography*, *39*(8), 1854–1870.
863 <https://doi.org/10.1175/2009JPO4160.1>
- 864 Holliday, N. P., Cunningham, S. A., Johnson, C., Gary, S. F., Griffiths, C., Read, J. F., &
865 Sherwin, T. (2015). Multidecadal variability of potential temperature, salinity, and
866 transport in the eastern subpolar North Atlantic. *Journal of Geophysical Research:*

- 867 *Oceans*, 120(9), 5945–5967. <https://doi.org/10.1002/2015JC010762>
- 868 Holliday, N. P., Bersch, M., Berx, B., Chafik, L., Cunningham, S., Florindo-López, C., et
869 al. (2020). Ocean circulation causes the largest freshening event for 120 years in
870 eastern subpolar North Atlantic. *Nature Communications*, 11(1), 585.
871 <https://doi.org/10.1038/s41467-020-14474-y>
- 872 Houpert, L., Inall, M. E., Dumont, E., Gary, S., Johnson, C., Porter, M., et al. (2018).
873 Structure and Transport of the North Atlantic Current in the Eastern Subpolar Gyre
874 From Sustained Glider Observations. *Journal of Geophysical Research: Oceans*,
875 123(8), 6019–6038. <https://doi.org/10.1029/2018JC014162>
- 876 Howe, J. A., Stoker, M. S., & Woolfe, K. J. (2001). Deep-marine seabed erosion and
877 gravel lags in the northwestern Rockall Trough, North Atlantic Ocean. *Journal of*
878 *the Geological Society*, 158(3), 427–438. <https://doi.org/10.1144/jgs.158.3.427>
- 879 Huthnance, J. M. (1984). Slope Currents and “JE BAR.” *Journal of Physical*
880 *Oceanography*, 14(4), 795–810. [https://doi.org/10.1175/1520-](https://doi.org/10.1175/1520-0485(1984)014<0795:SCA>2.0.CO;2)
881 [0485\(1984\)014<0795:SCA>2.0.CO;2](https://doi.org/10.1175/1520-0485(1984)014<0795:SCA>2.0.CO;2)
- 882 Johnson, C., Sherwin, T., Smythe-Wright, D., Shimmield, T., & Turrell, W. (2010).
883 Wyville Thomson Ridge Overflow Water: Spatial and temporal distribution in the
884 Rockall Trough. *Deep-Sea Research Part I: Oceanographic Research Papers*,
885 57(10), 1153–1162. <https://doi.org/10.1016/j.dsr.2010.07.006>
- 886 Johnson, C., Sherwin, T., Cunningham, S., Dumont, E., Houpert, L., & Holliday, N. P.
887 (2017). Transports and pathways of overflow water in the Rockall Trough. *Deep*
888 *Sea Research Part I: Oceanographic Research Papers*, 122, 48–59.
889 <https://doi.org/10.1016/j.dsr.2017.02.004>
- 890 Lozier, M. S., Li, F., Bacon, S., Bahr, F., Bower, A. S., Cunningham, S. A., et al. (2019).
891 A sea change in our view of overturning in the subpolar North Atlantic. *Science*,
892 363(6426), 516–521. <https://doi.org/10.1126/science.aau6592>
- 893 Marsh, R., Haigh, I. D., Cunningham, S. A., Inall, M. E., Porter, M., & Moat, B. I. (2017).
894 Large-scale forcing of the European Slope Current and associated inflows to the
895 North Sea. *Ocean Science*, 13(2), 315–335. <https://doi.org/10.5194/os-13-315->

- 896 2017
- 897 McCarthy, G. D., Smeed, D. A., Johns, W. E., Frajka-Williams, E., Moat, B. I., Rayner,
898 D., et al. (2015). Measuring the Atlantic Meridional Overturning Circulation at 26°N.
899 *Progress in Oceanography*, *130*, 91–111.
900 <https://doi.org/10.1016/j.pocean.2014.10.006>
- 901 Mercier, H., Lherminier, P., Sarafanov, A., Gaillard, F., Daniault, N., Desbruyères, D., et
902 al. (2015). Variability of the meridional overturning circulation at the Greenland-
903 Portugal OVIDE section from 1993 to 2010. *Progress in Oceanography*, *132*, 250–
904 261. <https://doi.org/10.1016/j.pocean.2013.11.001>
- 905 Østerhus, S., Woodgate, R., Valdimarsson, H., Turrell, B., de Steur, L., Quadfasel, D.,
906 et al. (2019). Arctic Mediterranean exchanges: a consistent volume budget and
907 trends in transports from two decades of observations. *Ocean Science*, *15*(2), 379–
908 399. <https://doi.org/10.5194/os-15-379-2019>
- 909 Pollard, R. T., Read, J. F., Holliday, N. P., & Leach, H. (2004). Water masses and
910 circulation pathways through the Iceland basin during Vivaldi 1996. *Journal of*
911 *Geophysical Research C: Oceans*, *109*(4), 1–10.
912 <https://doi.org/10.1029/2003JC002067>
- 913 Pujol, M.-I. I., Faugère, Y., Taburet, G., Dupuy, S., Pelloquin, C., Ablain, M., & Picot, N.
914 (2016). DUACS DT2014: the new multi-mission altimeter data set reprocessed over
915 20 years. *Ocean Science*, *12*(5), 1067–1090. [https://doi.org/10.5194/os-12-1067-](https://doi.org/10.5194/os-12-1067-2016)
916 2016
- 917 Rayner, D., Hirschi, J. J. M., Kanzow, T., Johns, W. E., Wright, P. G., Frajka-Williams,
918 E., et al. (2011). Monitoring the Atlantic meridional overturning circulation. *Deep*
919 *Sea Research Part II: Topical Studies in Oceanography*, *58*(17–18), 1744–1753.
920 <https://doi.org/10.1016/j.dsr2.2010.10.056>
- 921 Reverdin, G., Niiler, P. P., & Valdimarsson, H. (2003). North Atlantic Ocean surface
922 currents. *Journal of Geophysical Research C: Oceans*, *108*(1), 2–1.
923 <https://doi.org/10.1029/2001jc001020>
- 924 Rossby, T., & Flagg, C. N. (2012). Direct measurement of volume flux in the Faroe-

- 925 Shetland Channel and over the Iceland-Faroe Ridge. *Geophysical Research*
926 *Letters*, 39(7), n/a-n/a. <https://doi.org/10.1029/2012GL051269>
- 927 Sarafanov, A., Falina, A., Mercier, H., Sokov, A., Lherminier, P., Gourcuff, C., et al.
928 (2012). Mean full-depth summer circulation and transports at the northern periphery
929 of the Atlantic Ocean in the 2000s. *Journal of Geophysical Research: Oceans*,
930 117(1), n/a-n/a. <https://doi.org/10.1029/2011JC007572>
- 931 Schmidtko, S., Johnson, G. C., & Lyman, J. M. (2013). MIMOC: A global monthly
932 isopycnal upper-ocean climatology with mixed layers. *Journal of Geophysical*
933 *Research: Oceans*, 118(4), 1658–1672. <https://doi.org/10.1002/jgrc.20122>
- 934 Sherwin, T. J., Griffiths, C. R., Inall, M. E., & Turrell, W. R. (2008). Quantifying the
935 overflow across the Wyville Thomson Ridge into the Rockall Trough. *Deep-Sea*
936 *Research Part I: Oceanographic Research Papers*, 55(4), 396–404.
937 <https://doi.org/10.1016/j.dsr.2007.12.006>
- 938 Souza, A. J., Simpson, J. H., Harikrishnan, M., & Malarkey, J. (2001). Flow structure
939 and seasonality in the Hebridean slope current. *Oceanologica Acta*, 24(SUPPL.),
940 63–76. [https://doi.org/10.1016/s0399-1784\(00\)01103-8](https://doi.org/10.1016/s0399-1784(00)01103-8)
- 941 Thurnherr, A.M., (2014). How to Process LADCP Data with the LDEO Software
942 (versions IX.7 IX.10),
943 [https://www.bodc.ac.uk/data/documents/nodb/pdf/ladcp_ideo_processing_IX.7_IX.](https://www.bodc.ac.uk/data/documents/nodb/pdf/ladcp_ideo_processing_IX.7_IX.10.pdf)
944 10.pdf
- 945 Volkov, D. L. (2005). Interannual Variability of the Altimetry-Derived Eddy Field and
946 Surface Circulation in the Extratropical North Atlantic Ocean in 1993–2001. *Journal*
947 *of Physical Oceanography*, 35(4), 405–426. <https://doi.org/10.1175/JPO2683.1>
- 948 Zhao, J., Bower, A., Yang, J., & Lin, X. (2018). Meridional heat transport variability
949 induced by mesoscale processes in the subpolar North Atlantic. *Nature*
950 *Communications*, 9(1), 1–9. <https://doi.org/10.1038/s41467-018-03134-x>

951

952

Figure1.

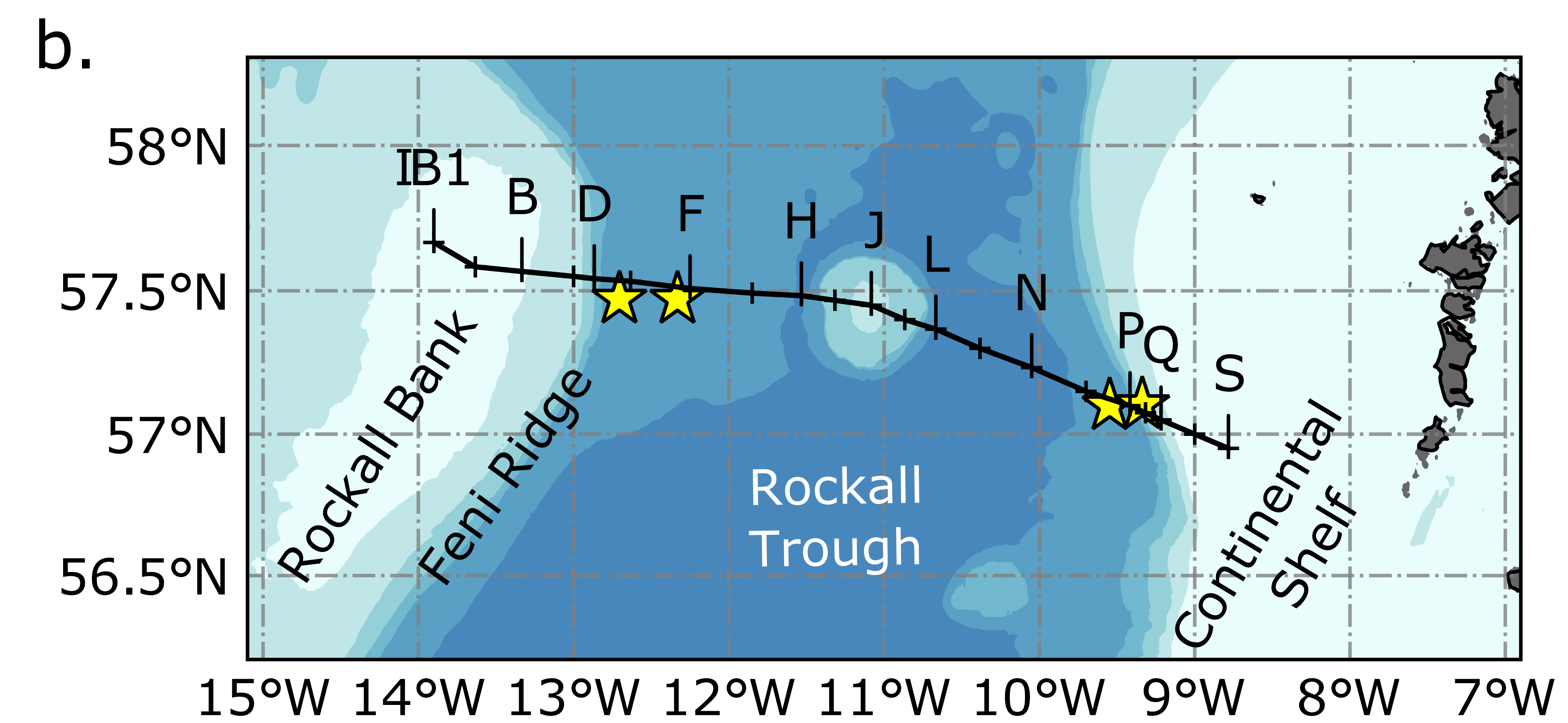
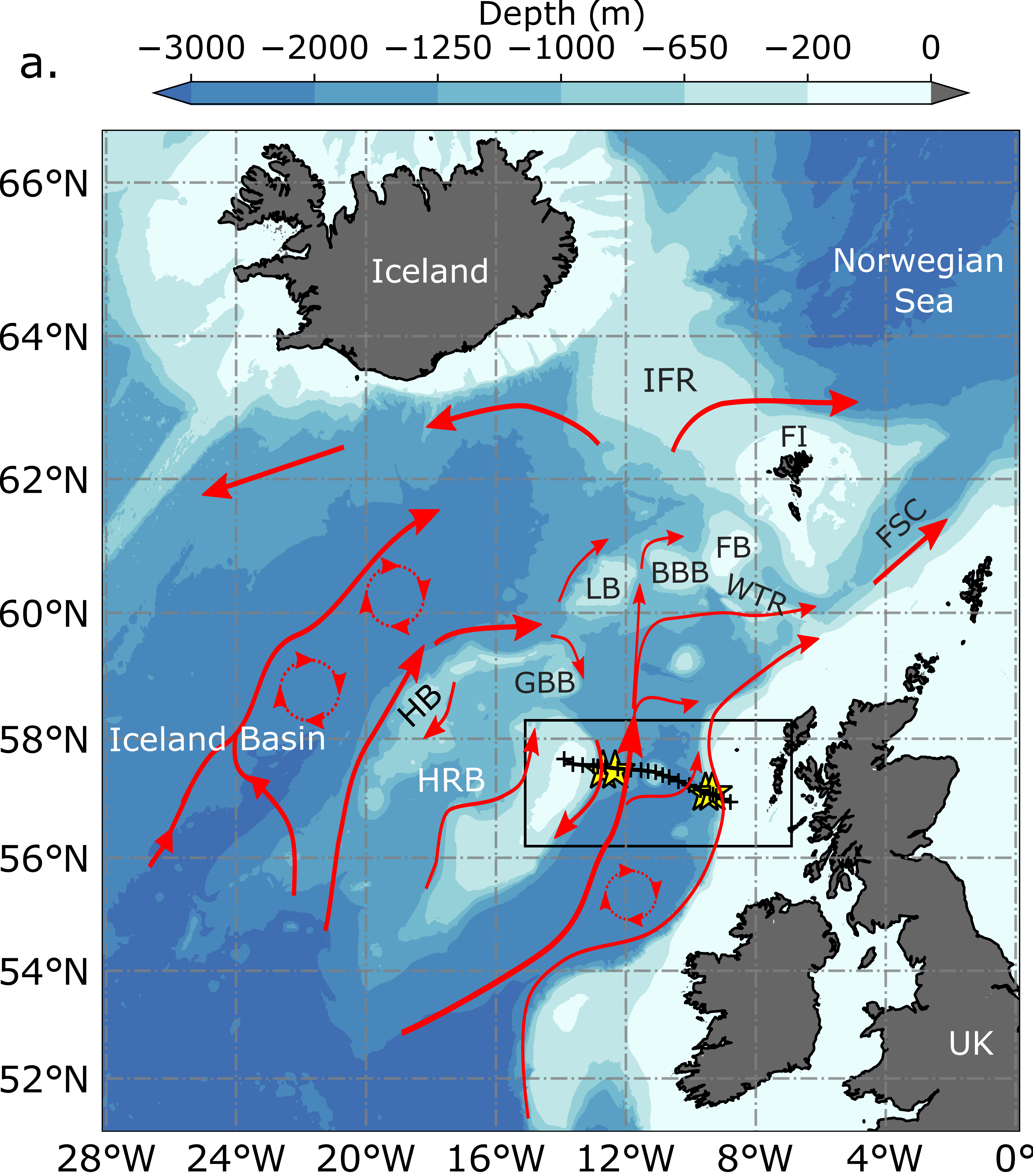


Figure2.

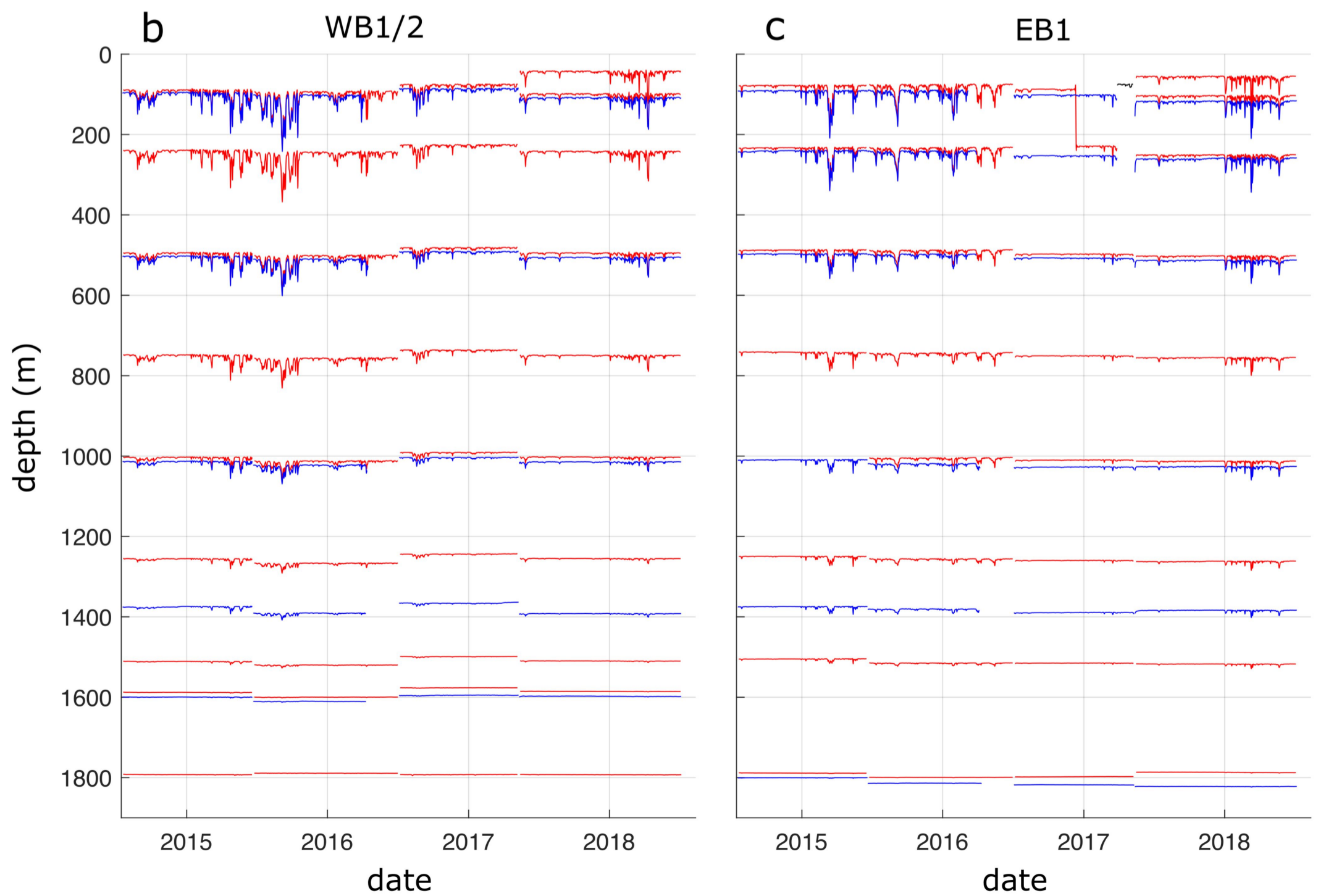
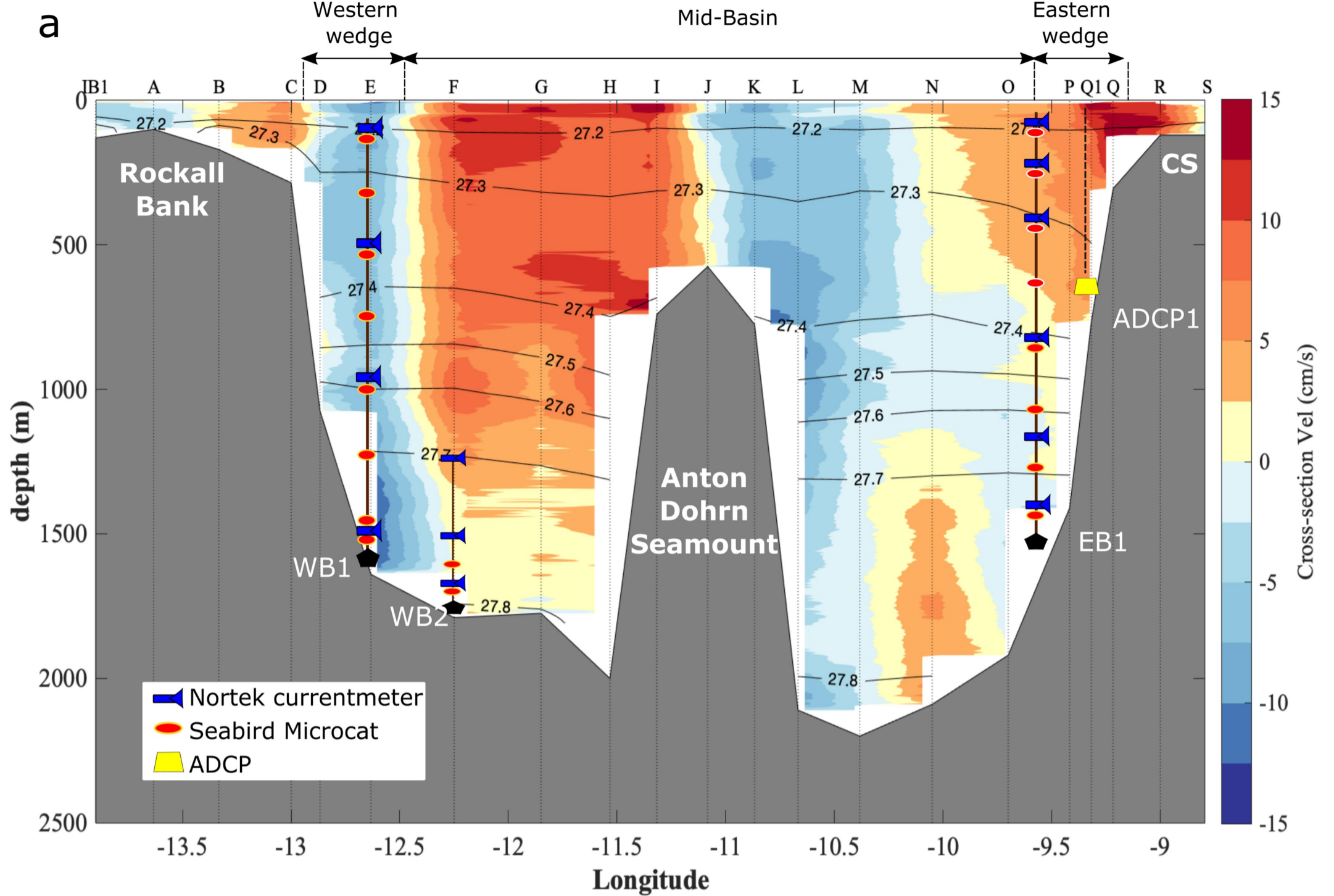
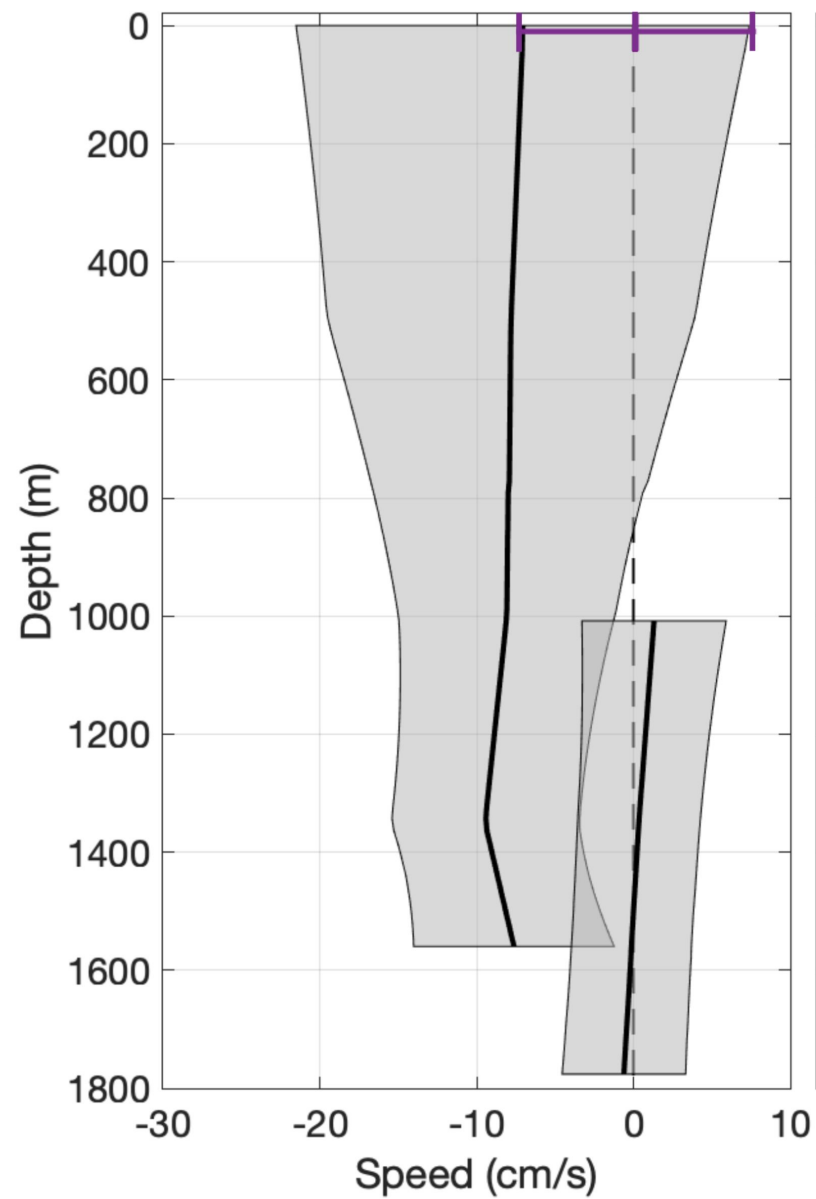
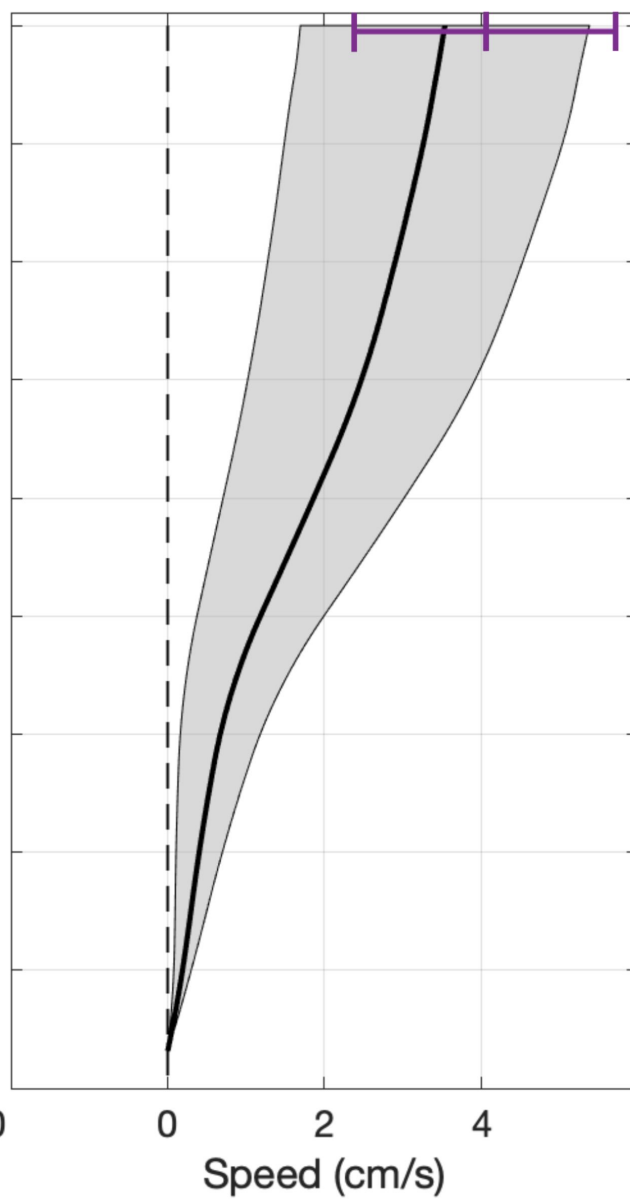


Figure 3.

a. WB1 and WB2



b. Mid-basin



c. EB1 and ADCP1

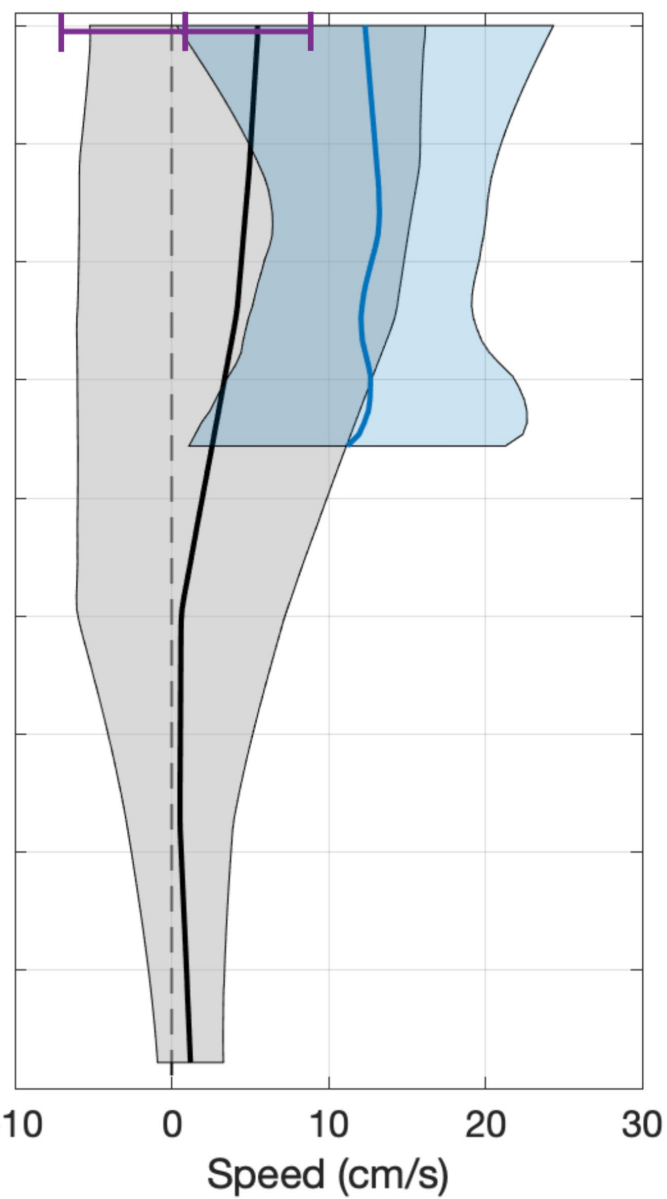


Figure4.

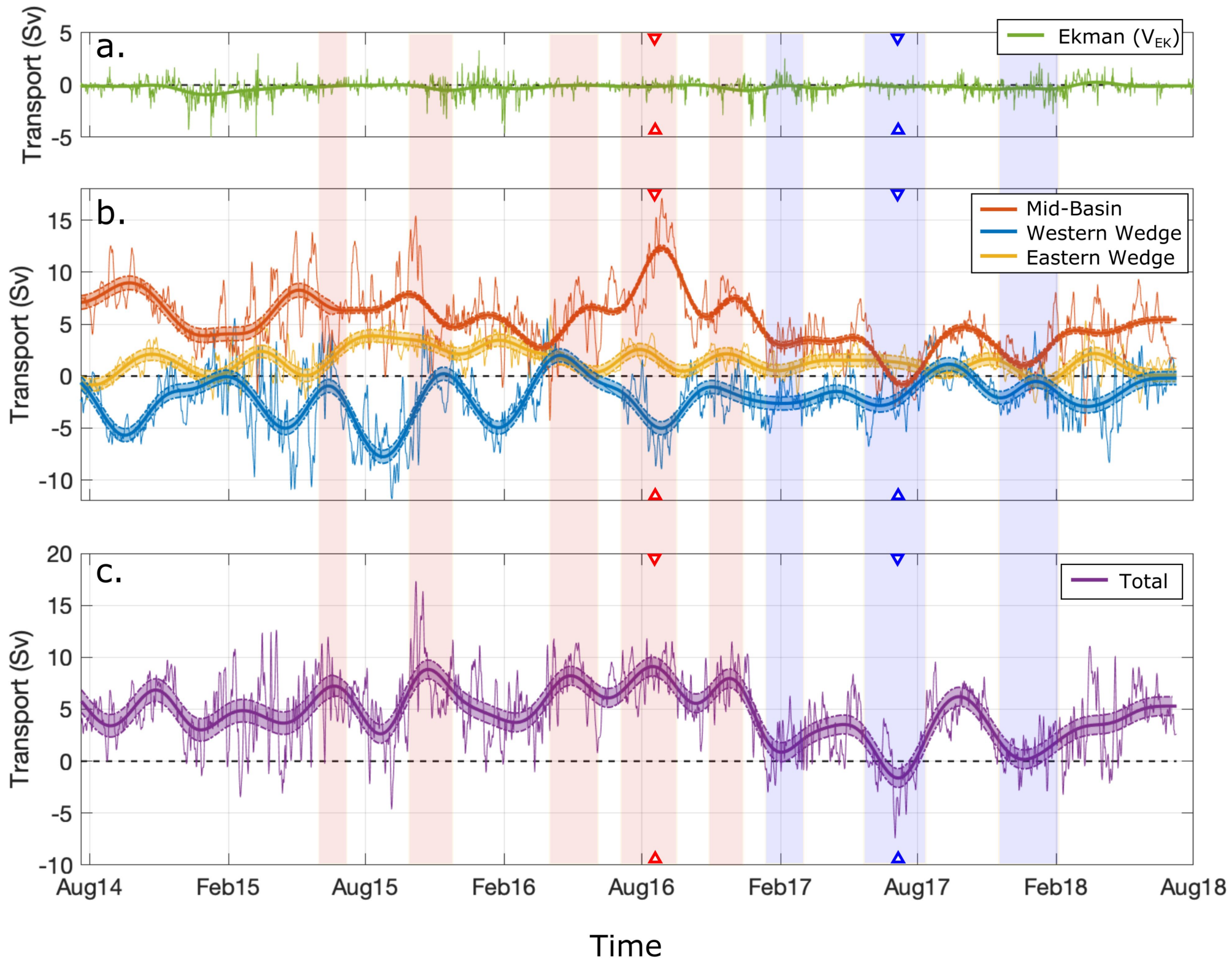


Figure 5.

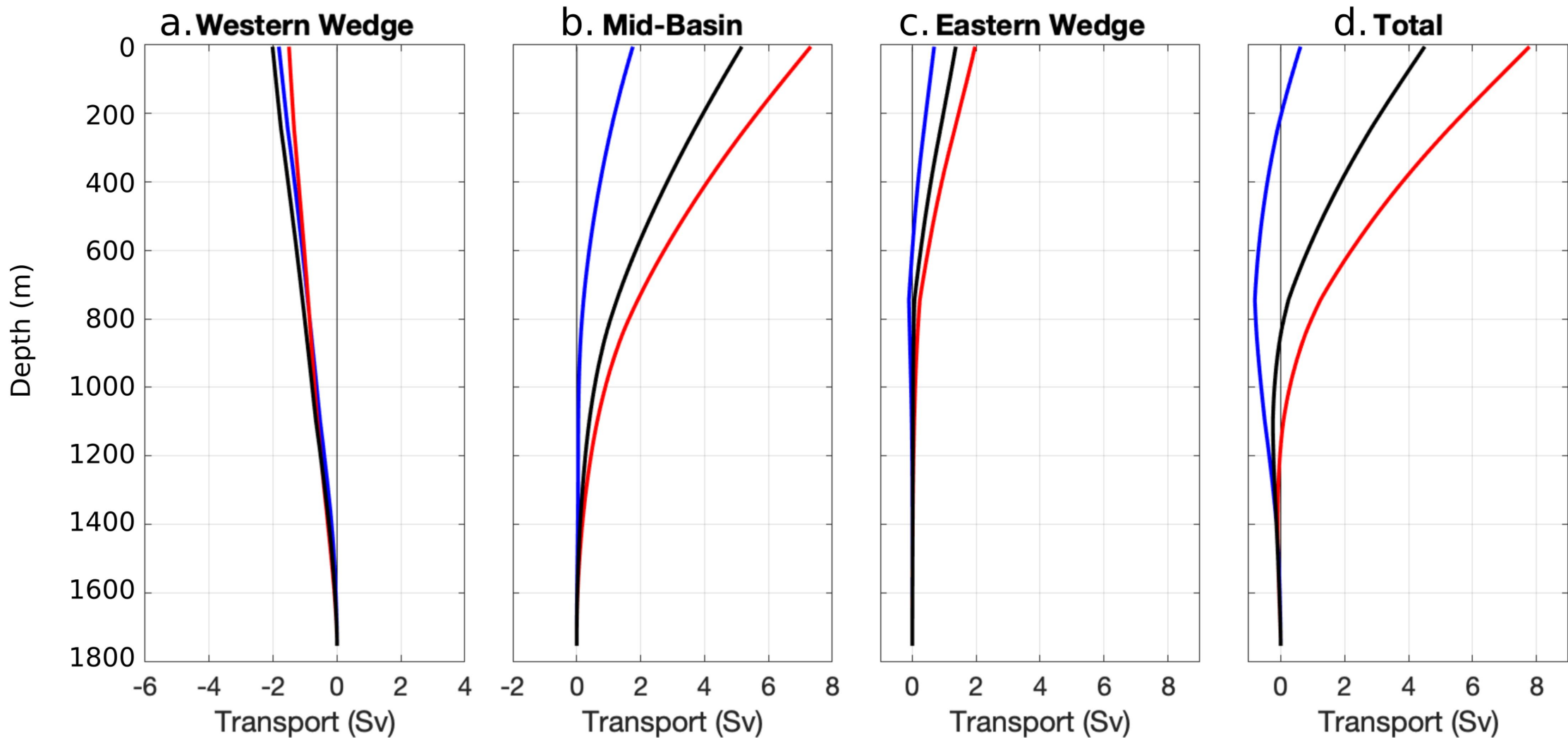


Figure6.

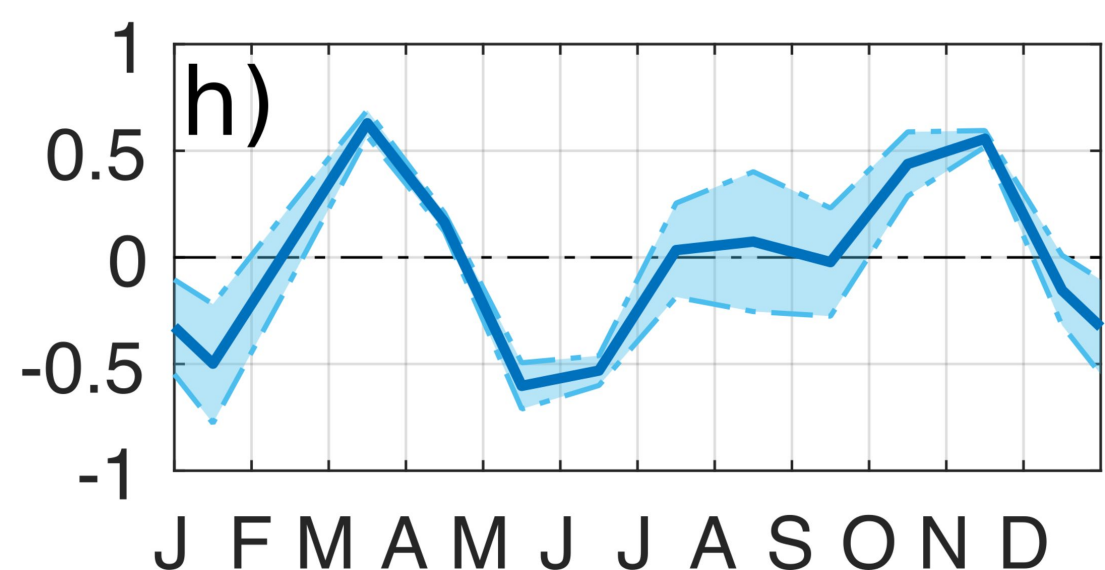
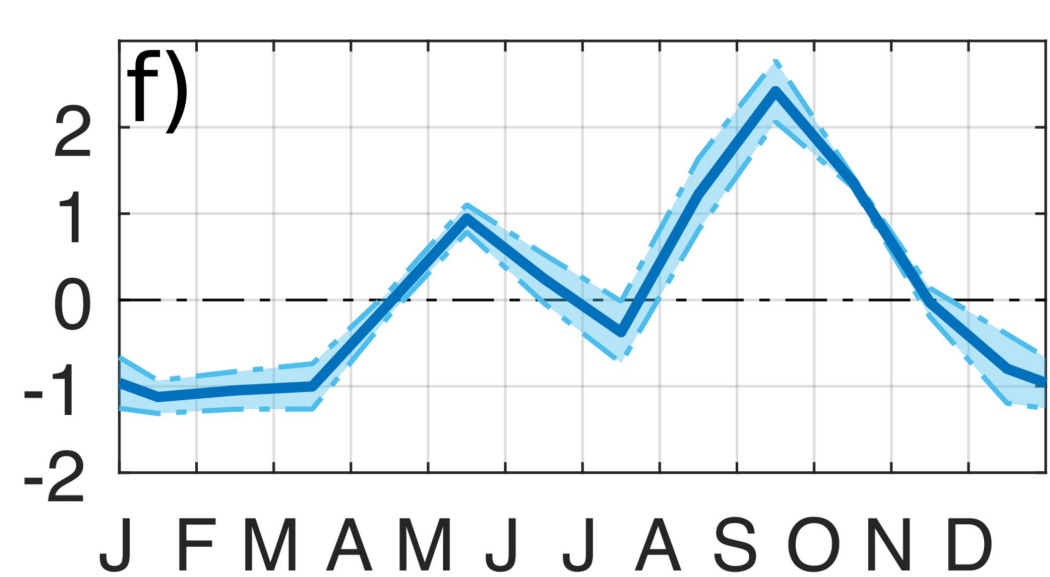
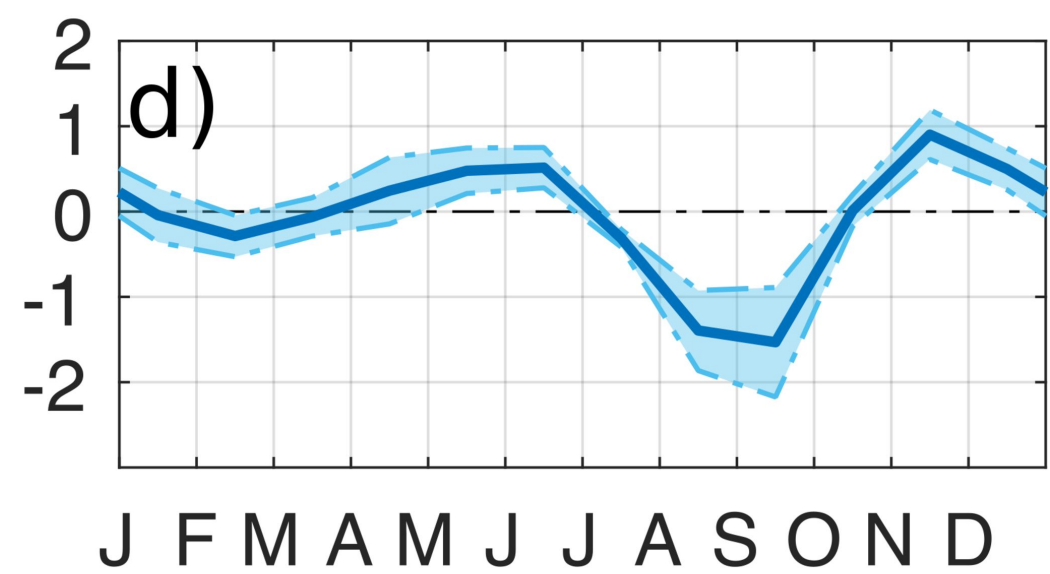
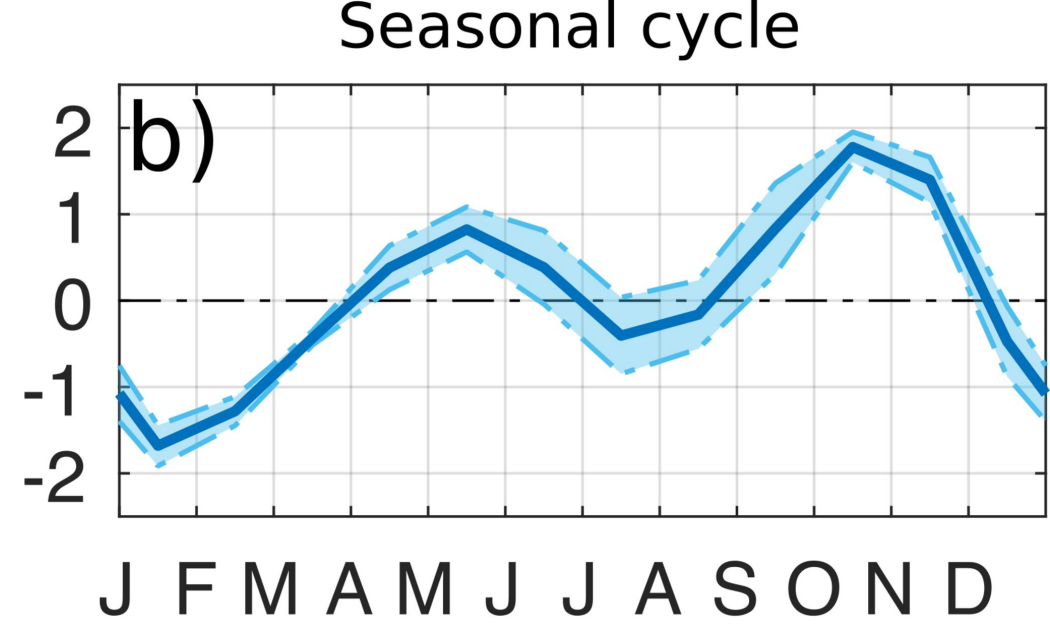
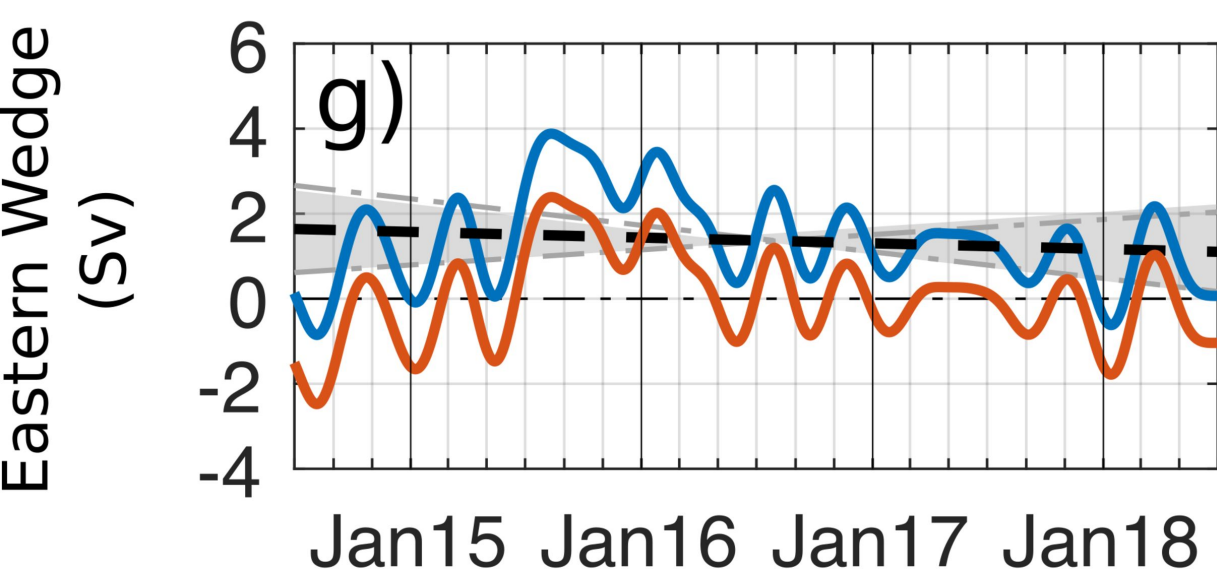
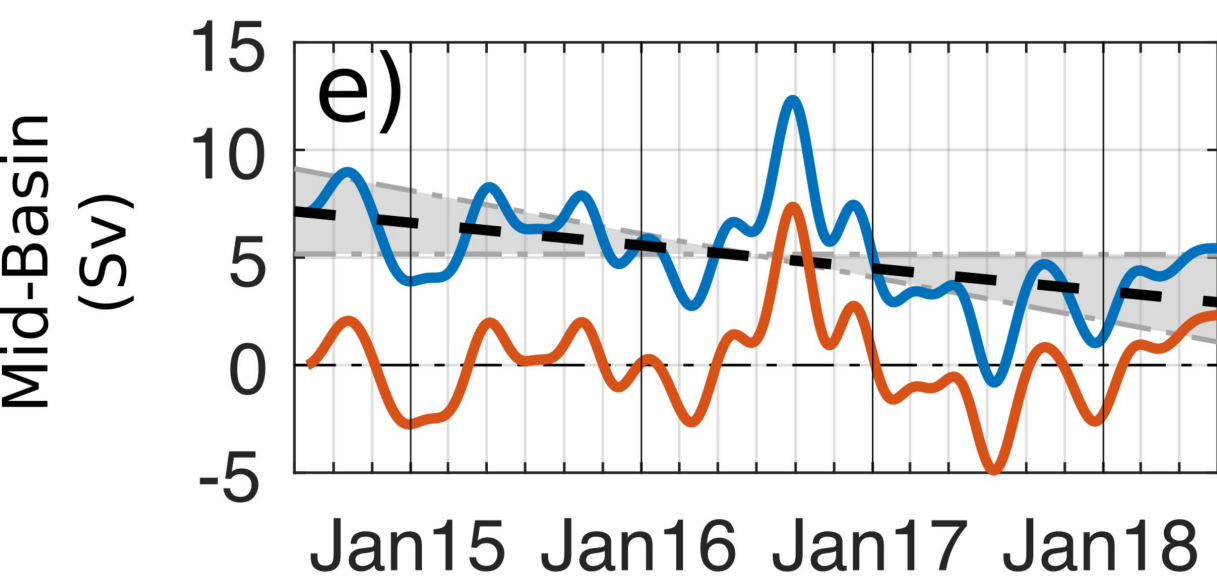
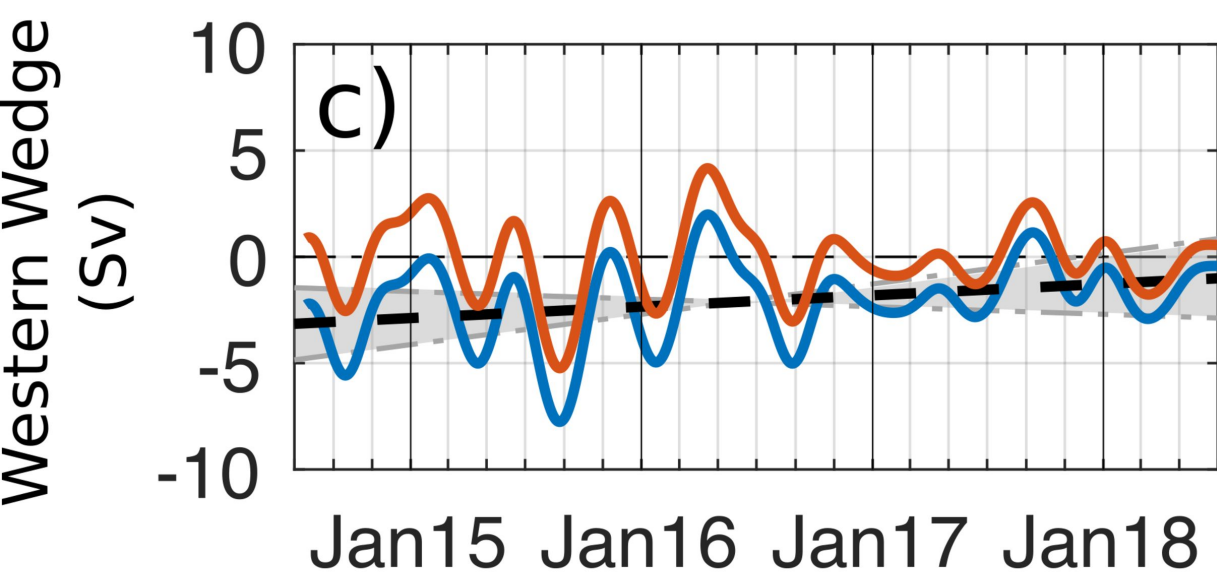
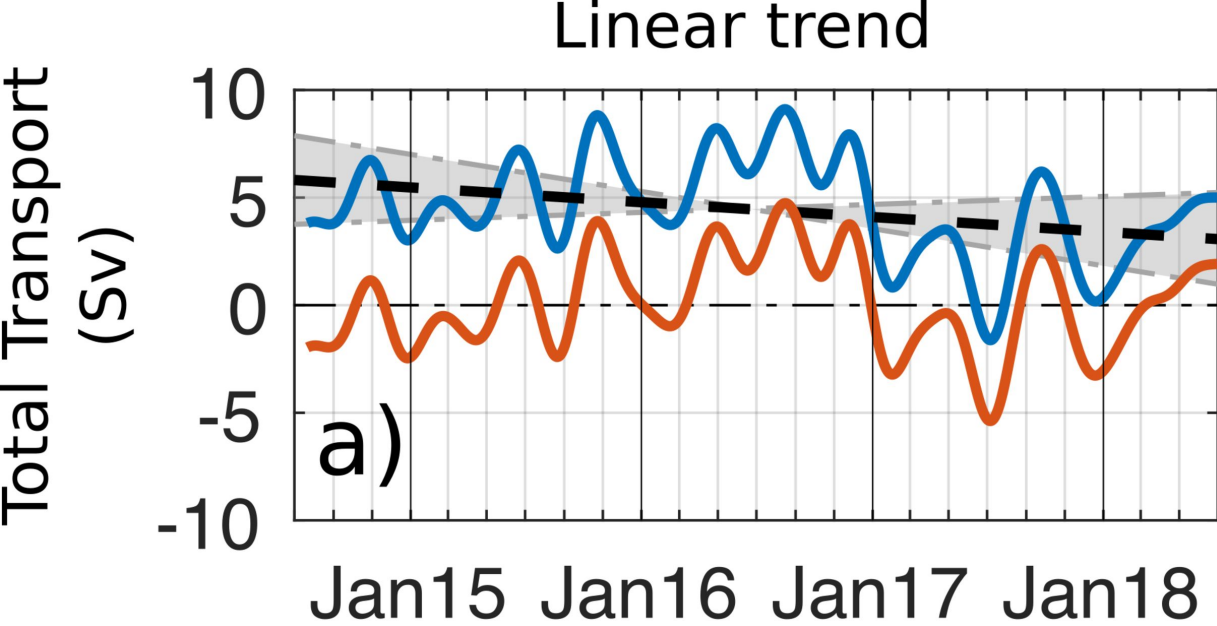
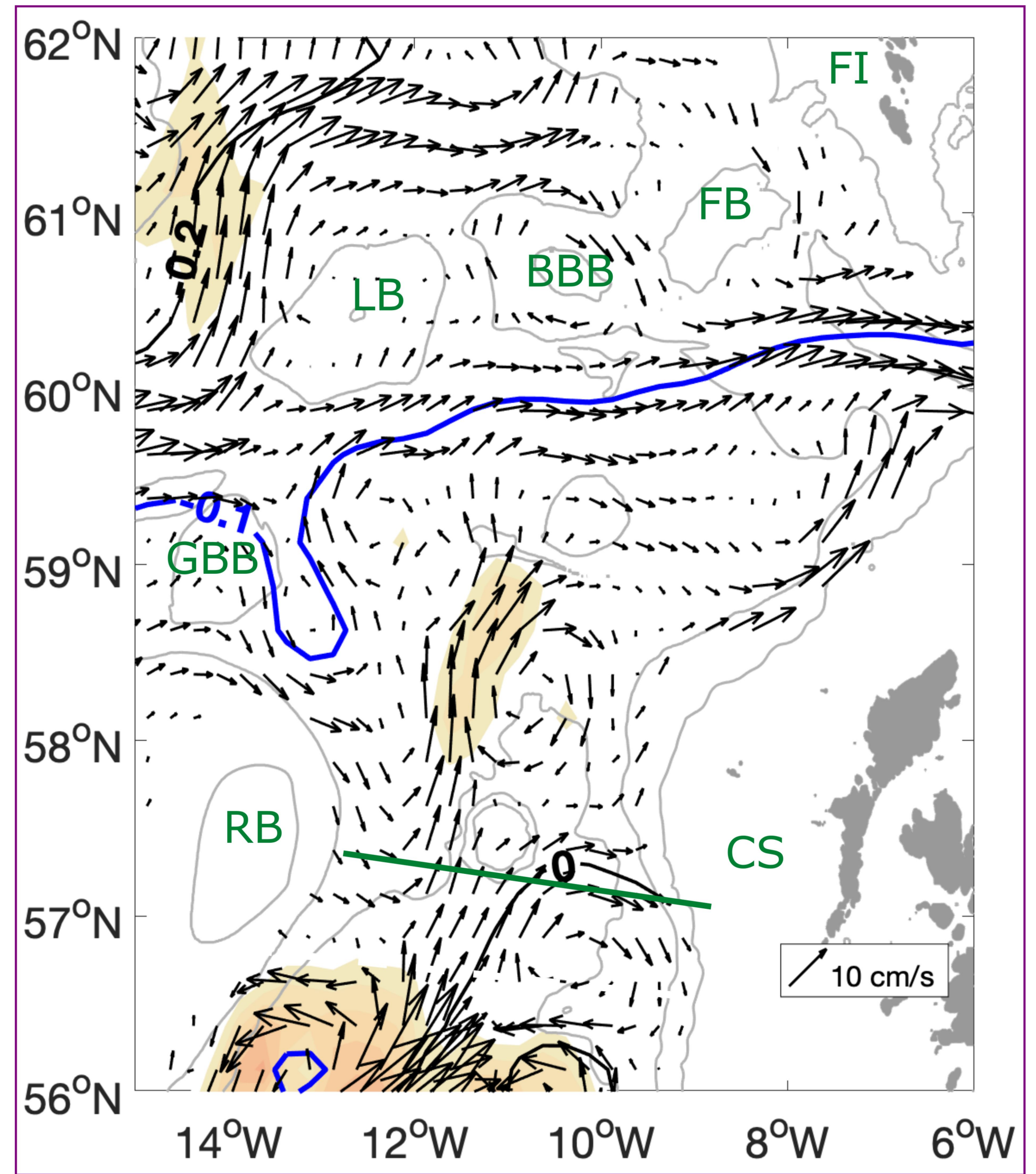
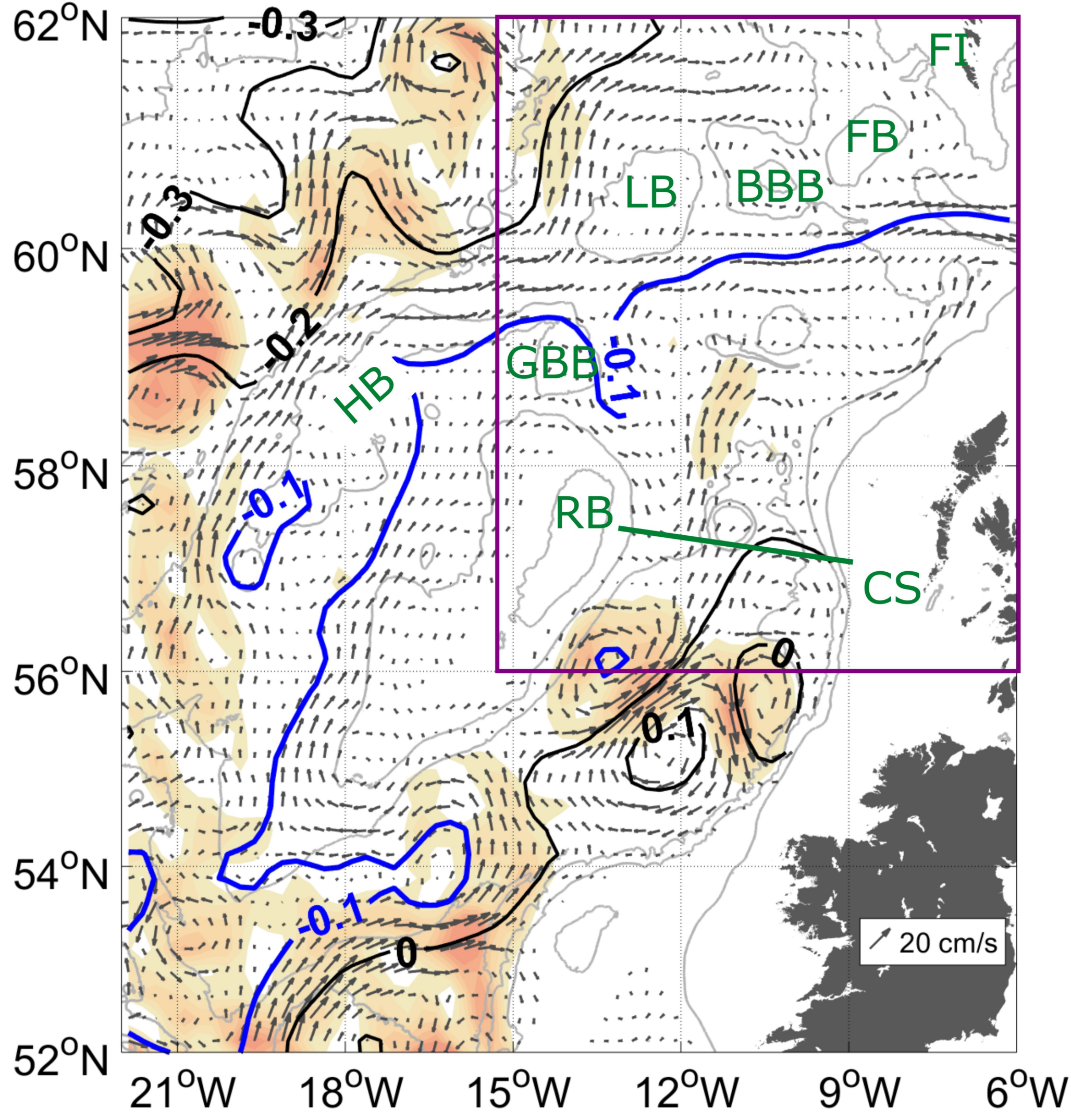
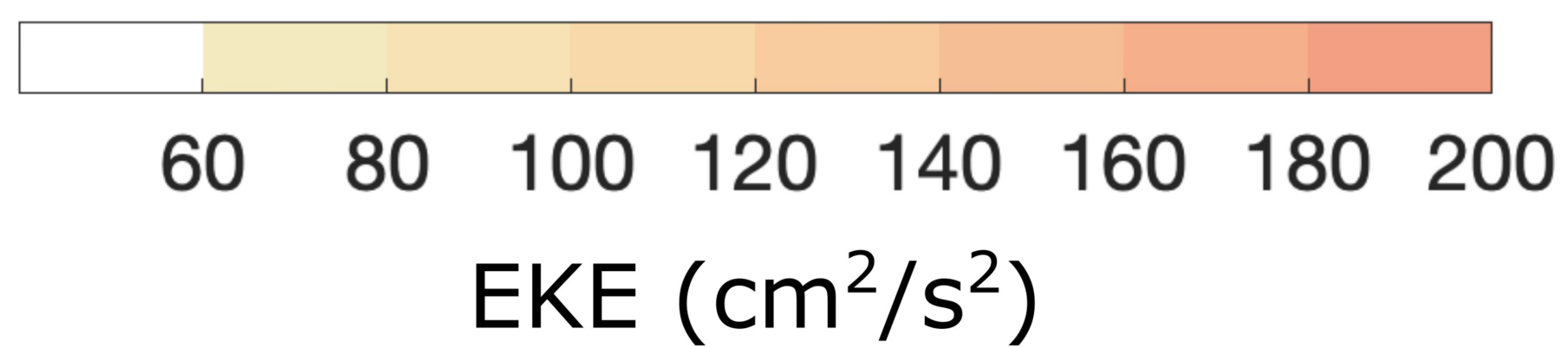
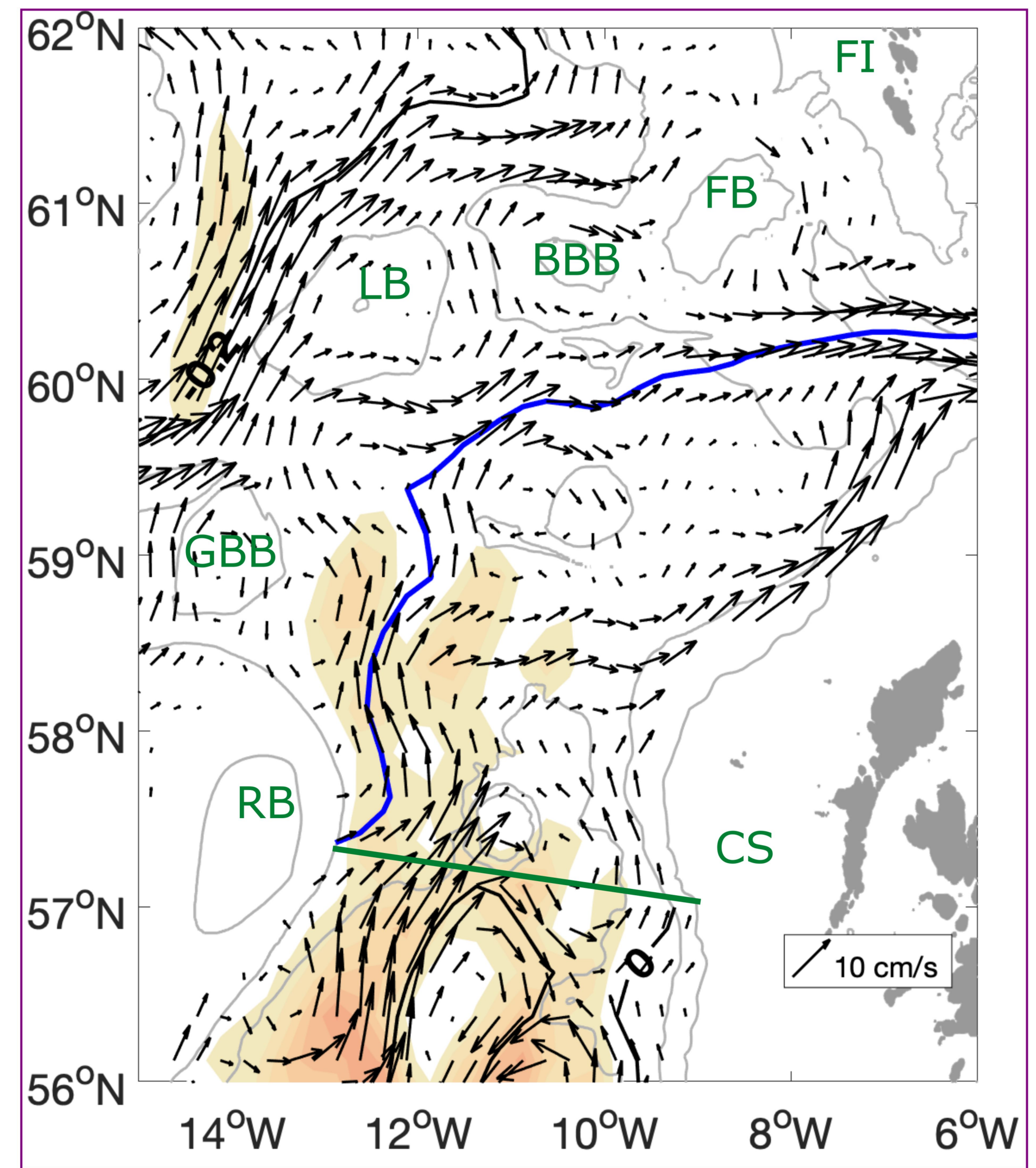
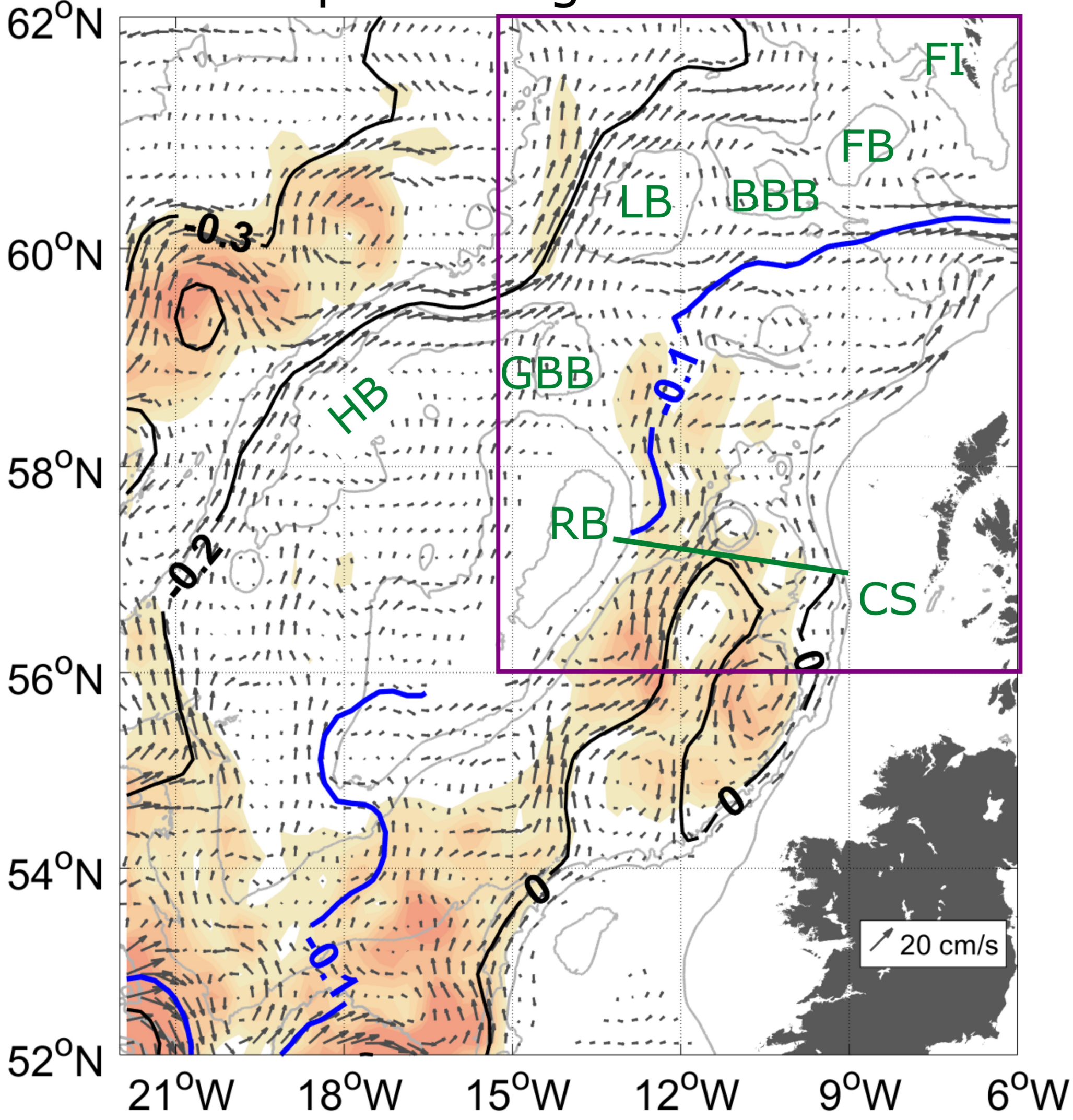


Figure 7.

a. Composite Low



b. Composite High



FigureA!

